ER Membrane Phospholipids and Surface Tension Control Cellular Lipid Droplet Formation

Kalthoum Ben M'barek,[1] Dalila Ajjaji,[1] Aymeric Chorlay,[1] Stefano Vanni,[2] Lionel Forêt,[1] and Abdou Rachid Thiam[1,3,*]
[1]Laboratoire de Physique Statistique, Département de Physique de l'ENS, École Normale Supérieure, PSL Research University, Université Paris Diderot, Sorbonne Paris Cité, Sorbonne Universités, UPMC Université Paris 06, CNRS, 75005 Paris, France
[2]Department of Biology, University of Fribourg, 1700 Fribourg, Switzerland
[3]Lead Contact
*Correspondence: thiam@lps.ens.fr

SUMMARY

Cells convert excess energy into neutral lipids that are made in the endoplasmic reticulum (ER) bilayer. The lipids are then packaged into spherical or budded lipid droplets (LDs) covered by a phospholipid monolayer containing proteins. LDs play a key role in cellular energy metabolism and homeostasis. A key unanswered question in the life of LDs is how they bud off from the ER. Here, we tackle this question by studying the budding of artificial LDs from model membranes. We find that the bilayer phospholipid composition and surface tension are key parameters of LD budding. Phospholipids have differential LD budding aptitudes, and those inducing budding decrease the bilayer tension. We observe that decreasing tension favors the egress of neutral lipids from the bilayer and LD budding. In cells, budding conditions favor the formation of small LDs. Our discovery reveals the importance of altering ER physical chemistry for controlled cellular LD formation.

INTRODUCTION

Nearly all cells and organisms are able to store excess nutrients so as to buffer energy fluxes. In storage conditions, nutrients are transformed into neutral lipids (oils) such as triglycerides, sterol esters, or squalene, which are packaged into organelles called lipid droplets (LDs) (Martin and Parton, 2006). LDs are dynamic organelles playing a central role in cellular lipid metabolism and homeostasis (Walther and Farese, 2012). LD full function is yet more complex than currently known, as illustrated by the expanding list of unforeseen implications of LD in cell biology (Welte, 2015).

Despite their multiple functions, how LDs form is poorly understood (Pol et al., 2014; Thiam and Beller, 2017; Wilfling et al., 2014a). LD biogenesis starts in the endoplasmic reticulum (ER) wherein a cascade of enzymatic reactions mediates the synthesis of neutral lipids that are encapsulated within the ER intermonolayer space. At a critical concentration, the lipids presumably demix from the ER membrane to nucleate a lipid lens (i.e., gathering of the lipids into a lens-like shape) (Choudhary et al., 2015; Pol et al., 2014; Thiam and Foret, 2016). By acquiring more neutral lipids, the lens grows and buds into a spherical LD that is covered by a phospholipid monolayer containing proteins.

How LDs bud off from the ER is barely understood (Guo et al., 2009; Ohsaki et al., 2014). Whether proteins at the LD surface can physically bud LDs from the ER, similarly to coat-induced vesicle budding, is unknown (Ohsaki et al., 2014). Another hypothesis suggests that LDs undergo spontaneous structural shape changes in the ER to become spherical (Guo et al., 2009; Ohsaki et al., 2014; Pol et al., 2014), but the mechanical basis for this membrane remodeling is also unclear. Related to this model, LD may spontaneously bud from the ER depending on the affinity of the neutral lipids with the ER bilayer (Thiam and Foret, 2016). Which of these two main models best describes LD formation is not known thus far.

Currently a group of proteins, including for example Seipin or the fat storage-inducing transmembrane proteins, has been identified as important for LD formation (Cartwright et al., 2015; Choudhary et al., 2015; Pol et al., 2014; Szymanski et al., 2007; Wang et al., 2016). These proteins probably regulate different steps in LD formation up to LD budding, but their exact functions are still unclear. Interestingly, except for ER enzymes that are implicated in the synthesis of neutral lipids and thereby provide materials for making LDs, there are no other proteins whose absence from all cell lines examined completely abolishes LD formation (Guo et al., 2008). This even encompasses perilipins, which are the most abundant LD proteins. The phenotype associated with the single deletion of a gene encoding a protein associated with LD formation or regulation is often a change in LD size and number (Guo et al., 2008; Yang et al., 2012). Across various cell lines, the deletion of specific genes associated with LD formation or regulation can additionally cause significant accumulation of neutral lipids in the ER bilayer (Adeyo et al., 2011; Gubern et al., 2008; Kadereit et al., 2008; Yang et al., 2012). These observations support the notion that a redundant combination of proteins are necessary to physically bud LD from the ER or proteins simply modulate other factors such as lipids or membrane physical properties that may govern the mechanical formation of LDs (Thiam and Foret, 2016).

As oil droplets, covered by a phospholipid monolayer in the cytosol, LDs can be seen as the disperse phase of an emulsion (i.e., oil-in-water droplets) (Thiam et al., 2013b). Consequently, LDs have particular interfacial properties as compared with the bilayer interface that surrounds most cellular organelles.

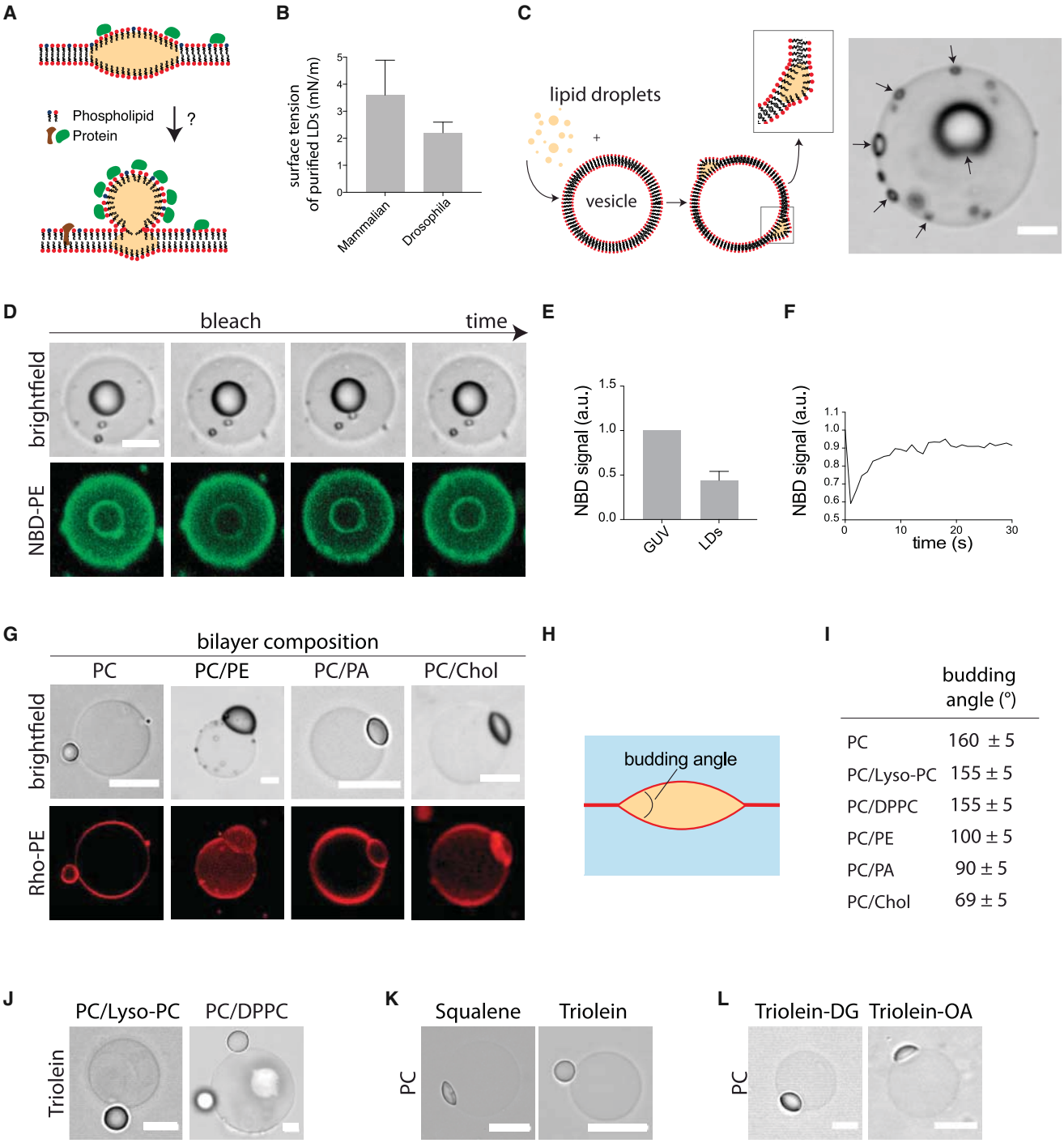

Figure 1. Lipids, Not Coat Proteins, Can Physically Mediate LD Budding

(A) Illustration of lipid droplet (LD) budding step. The contribution of proteins and lipids on LD budding is unknown.

(B) Surface tension values of LDs purified from mammalian (Cos 7) and *Drosophila* (Kc167) cells (Figure S1). Error bars represent the SD.

(C) Reconstitution of the LD formation topology in the ER. Giant unilamellar vesicles (GUVs) are mixed with artificial LDs that are included in the intermonolayer space of the GUV membrane. A bright-field image of the resulting product is shown: many artificial LDs depicted by the arrows are embedded in the bilayer. The bigger LD is on the apex of the GUV because of buoyancy difference with water. Scale bar, 10 μm.

(D) The NBD-DOPE signal of a GUV relocates to the artificial LD. The droplet is on the apex of the GUV. Scale bar, 10 μm.

(E) The signal of the artificial LD is twice as low as the signal of the GUV. Error bars represent the SD.

(F) Completely photobleaching the artificial LD signal leads to recovery, demonstrating the continuity between the GUV and the artificial LD.

(legend continued on next page)

For example, creating an interface between oil and water has a considerable energy cost because of the immiscibility of the two fluids (Thiam et al., 2013b). The parameter describing this energy cost is termed surface tension, which is the energy cost per generated area between the two phases (Penno et al., 2013; Thiam et al., 2013b). To minimize energy, surface tension will minimize the contact area between oil and water, which is attained by making droplets spherical. Thus, in the context of LD budding from the ER, surface tension can be expected to play an important role. However, the implication of surface tension in LD formation has not been explored so far (Thiam and Foret, 2016).

Here, we investigate the mechanism of LD budding from the ER membrane. We developed model systems reconstituting LD formation topology, and provide evidence that ER membrane phospholipids and surface tension are key parameters of LD formation. LD spherical formation is a spontaneous process determined by these parameters. Our results highlight the importance of remodeling ER lipid composition and tension for controlled cellular LD formation.

RESULTS

A Vesicular Budding Model for LD Formation Is Energetically Too Costly

In the coat-induced budding model (Figure 1A), the lateral interaction energy per area between two proteins has to be larger than the membrane surface tension (Chernomordik and Kozlov, 2003), which is the energy per created area between two compartments. Coat proteins such as clathrin or complex protein I polymerize to induce budding. The energy they provide should reflect the amount of energy required for proteins to mediate LD budding.

The interaction energy between clathrin proteins, or complex protein I coat proteins, is in the range of 0.1–0.5 mN/m (Chernomordik and Kozlov, 2003; Foret, 2014; Saleem et al., 2015; Thiam and Pincet, 2015). For the vesicular budding model of LDs to be possible, these values have to be larger than the surface tension of LDs. By using microaspiration techniques, we measured the surface tension of LDs purified from mammalian and *Drosophila* cells. The tension values were above 2 mN/m (Figure 1B), much larger than the interaction energy between coat proteins. Consequently, LD budding from the ER by coat-like proteins is unlikely. For illustration, budding a 100-nm-sized LD would require an energy input of over 10^4 k_BT at least (Figure S1B), while complex protein I, for example, can only provide at maximum $\sim 2 \times 10^3$ k_BT (Thiam and Pincet, 2015).

In Vitro Reconstitution of LD Formation

We next focused on the alternative mechanism by which neutral lipids would naturally assemble and adopt a spherical shape. We tested this hypothesis in vitro. We made giant unilamellar vesicles (GUVs) and mixed them with artificial LDs, which were incorporated into the intermonolayer space of the GUV membrane (Figures 1C, S1C, and S1D). Indeed, by making GUVs containing fluorescent phospholipids, the fluorescence partitioned to the artificial LDs. We observed 2-fold less fluorescence signal on the LD than on the GUV, showing that the LD is covered by a single phospholipid monolayer (Figures 1D and 1E). In addition, LD recovered fluorescence following complete photobleaching of the fluorophore (Figures 1D and 1F; Movie S1), proving that there is continuity between the GUV bilayer and the LD monolayer. Based on these observations, we think that this system reproduces well the topology of LD formation.

We next made GUVs containing various phospholipids and mixtures thereof, and added artificial LDs (Figures 1G and S1C). Alternatively, we made GUVs of fixed phospholipid composition and then added artificial LDs that contained the phospholipid of interest (Figure S1D). With both strategies, we observed that the artificial LDs had different budding shapes that depended on the phospholipid and neutral lipid composition (Figures 1G and 1J–1L). To characterize the droplet shape, e.g., the budding shape, we defined the budding angle as the angle formed between the two monolayers enclosing the oil phase (Figure 1H). A small angle corresponds to a lens-shaped LD, whereas formation of a spherical LD, which we call here LD budding, requires a budding angle close to 180°.

For artificial LDs made of triolein (one of the main triglycerides in cellular LDs), when GUVs were composed of phosphatidylcholine (PC) or a mixture of PC and lyso-phosphatidylcholine (Lyso-PC), the LDs adopted a budded shape (Figure 1J). In contrast, when the GUVs contained a mixture of PC and phosphatidylethanolamine (PE), or PC and phosphatidic acid (PA), the artificial LDs did not bud (Figure 1G). Moreover, in PC GUVs, squalene-containing artificial LDs did not bud, while triolein-containing LDs budded (Figure 1K). We studied other biologically relevant conditions and found various budding states depending on the lipid composition (Figures 1J and 1L). Finally, we found that altering the local concentration of lipids such as free fatty acids dynamically reformed the LD shape (Figures S1E and S1F; Movie S2). Our results therefore suggest that (1) LDs can spontaneously bud from the ER membrane, i.e., without the mechanical action of proteins, (2) ER phospholipids play a critical role in LD budding, and (3) phospholipids have different budding aptitudes.

(G) GUVs made with different phospholipids and mixtures thereof have different artificial droplet shapes. PC, phosphatidylcholine; PE, phosphatidylethanolamine; PA, phosphatidic acid; Chol, cholesterol. Rhodamine-PE is used to visualize the membranes by fluorescence. Representative images are shown for each condition. Scale bar, 10 μm.

(H) The budding shape is characterized by the budding angle: the angle formed between the two monolayers enclosing the lipid oil phase.

(I) The budding angles are determined for different phospholipid conditions and triolein as the neutral lipid phase: PC (n = 15), PC/PE (n = 12), PC-Lyso-PC (n = 12), PC/DPPC (n = 12), PC/PA (n = 20), and PC/Chol (n = 5).

(J) The artificial LDs are almost fully budded when the GUV bilayer is made of PC containing Lyso-PC or saturated PC (dipalmitic phosphatidylcholine). Scale bar, 10 μm.

(K) Squalene-containing artificial LDs are non-budded in PC GUVs while triolein LDs are budded. Scale bar, 10 μm.

(L) Dioleoyl glycerol (DG)- and oleic acid (OA)-containing artificial LDs are non-budded. Scale bar, 10 μm.

See also Figure S1; Movies S1 and S2.

Deciphering the Differential Budding Aptitudes of Phospholipids

The model vesicles difficultly formed with particular lipid compositions, and were often multilamellar. To be able to evaluate the individual budding capacity of each lipid component, we decided to switch to a more controllable system based on micrometric adhesive emulsion droplets (Figure 2A), termed droplet interface bilayer (Bayley et al., 2008; Poulin and Bibette, 1998; Thiam et al., 2011, 2012). The topology of these emulsion droplets recapitulates the configuration of an LD in the ER membrane, as the bilayer splits up into two monolayers covering oil (Figure 2A). The size and curvature of the buffer droplets do not affect the angle between the two monolayers (see STAR Methods). The angle of the droplet interface bilayer system thus describes the budding angle (Figure 2A) and the shape of a forming LD in a bilayer (Figure 2B). Formation of a spherical LD, called LD budding, also corresponds here to an angle close to 180° (Figure 2B).

Experimentally, we made buffer drops in neutral lipids containing lipid surfactants (i.e., amphiphilic molecules, including phospholipids) that absorbed to the surface of the drops and formed a monolayer (Figure 2A). When two drops were close enough to each other, they spontaneously formed a bilayer that is continuous with the two monolayers, resulting in a budding angle (Figure 2B and Movie S3). With this technique we wanted to determine the ability of various lipid surfactants to bud neutral lipids. We worked with PC, PE, PA, phosphaidylinositol (PI), 1-monooleoyl glycerol, 1,2-dioleoyl glycerol, cholesterol, and oleic acid. We varied the acyl chains of PC, testing dimyristelaidoyl PC (14:1, PC), dipalmitic PC, polyunsaturated PC, and Lyso-PC. Lyso-PC constituted a particular case as the buffer drops systematically fused; we chose to mix Lyso-PC with PA at 20:80, which was the maximum Lyso-PC amount that allowed the formation of stable droplet interface bilayers. All of these lipid surfactants are present in the ER membrane but at different levels, depending on the cell type or metabolic state; the differences between the phospholipids are their headgroups, or their acyl chain number, length, and saturation. For the neutral lipid phases we used triolein, a triolein-sterol ester mixture (75:25, w/w), and squalene (Figures 2C, 2D, and S2B). These neutral lipids are the most abundant ones and their concentrations in LDs depend on the cell type or metabolic condition.

For each neutral lipid and phospholipid combination, we measured the budding angle (Figures 2E, 2F, and S2C–S2D). We found three main classes of lipid surfactants and phospholipids (Figure 2E). First, saturated phospholipids, PI, and Lyso-PC met the budding condition for LDs containing any of the neutral lipids (Figure 2E). Second, PC and polyunsaturated phospholipids enabled the budding of specific neutral lipids (Figure 2E). For instance, consistently with Figure 1K, we observed that PC mediated the budding of triolein but not of squalene, or of sterol esters (Figure 2E). Third, lipids such as PE, PA, diacylglycerol, and cholesterol did not meet the budding requirement for any of the neutral lipids (Figure 2E). These results also show that, for a given neutral lipid composition, only specific phospholipids met the budding condition for LDs (Figure 2F).

This droplet interface bilayer approach enabled us to determine the individual contribution of each lipid surfactant and phospholipid on LD budding. Our observations on the differential budding aptitudes of phospholipids are consistent with the shapes of artificial LDs contained in GUVs (Figures 1G and 1I–1L). Altogether, the GUV and droplet interface bilayer experiments suggest that, when a given neutral lipid is synthesized in the ER, increasing the local concentration of specific phospholipids will allow to efficiently package the neutral lipids into spherical LDs.

Neutral Lipids Are Naturally Removed from the Bilayer under Budding Conditions

To make an LD, the neutral lipids in the ER must be removed from the bilayer and transferred into the forming LD. We thus asked whether the differential phospholipid budding aptitudes is related to a differential ability to remove neutral lipids from the bilayer for their packaging into droplets. To address this question we worked with triolein, the most abundant triglyceride, and PC and PE, the most abundant ER phospholipids. We made PE-droplet interface bilayers in a triolein environment containing fluorescent triolein-pyrene, which was used as a reporter for triolein localization (Figure 3A). We observed that PE, which did not promote budding (Figures 2E and 3A), tolerated triolein accumulation in the bilayer (Figure 3A and 3B); the triolein signal located in the bilayer was around 15% of the surrounding triolein signal (Figures 3B and 3E). When we instead used PC, which promoted budding (Figures 2E and 3C), triolein was absent from the bilayer (Figures 3C–3E), despite the massive surrounding triolein environment; similar observations were made with other budding phospholipids such as saturated phospholipids (not shown). Accordingly, we observed that PC/PE (50:50) GUVs containing artificial triolein LDs had more triolein signal in the bilayer than in PC GUVs (Figures S3E and S3F). These observations suggest that phospholipids have different aptitudes for removing neutral lipids from the ER bilayer. Importantly, the budding condition coincided with the egress of free neutral lipids from the bilayer (Figures 3C and 3D).

To follow the neutral lipid egress from the bilayer during budding, we made a droplet interface bilayer with PE and then added PC-in-triolein in the bulk phase (Figure 3F). We recorded the evolution of the triolein-pyrene signal in the bilayer and the budding angle. Over time we observed an increase of the budding angle, which was indicative of PC recruitment to the membranes (Figure S3G). In the meantime, the triolein-pyrene signal in the bilayer decreased (Figures 3F, 3G, and S3H). Consequently, based on the budding angle increase, these results support the conclusion that neutral lipids are naturally removed from the bilayer concomitantly with LD budding (Figure 3H). With lipid surfactants or phospholipids that do not promote budding, neutral lipids will accumulate in the bilayer.

The Decrease of the Bilayer Surface Tension Mediates Triolein Egress from the Bilayer and LD Budding

Our previous results support that the molecular affinities between neutral lipids and phospholipids are important for packaging the lipids and budding of LDs (Figures 1, 2, and 3). These molecular interactions are encompassed by the surface tension parameter, which is here the energy cost per generated area between two liquid phases. During LD formation, three surface tensions come into play (Figure 4A): the surface tension of the bilayer separating the ER lumen and the cytosol, the surface

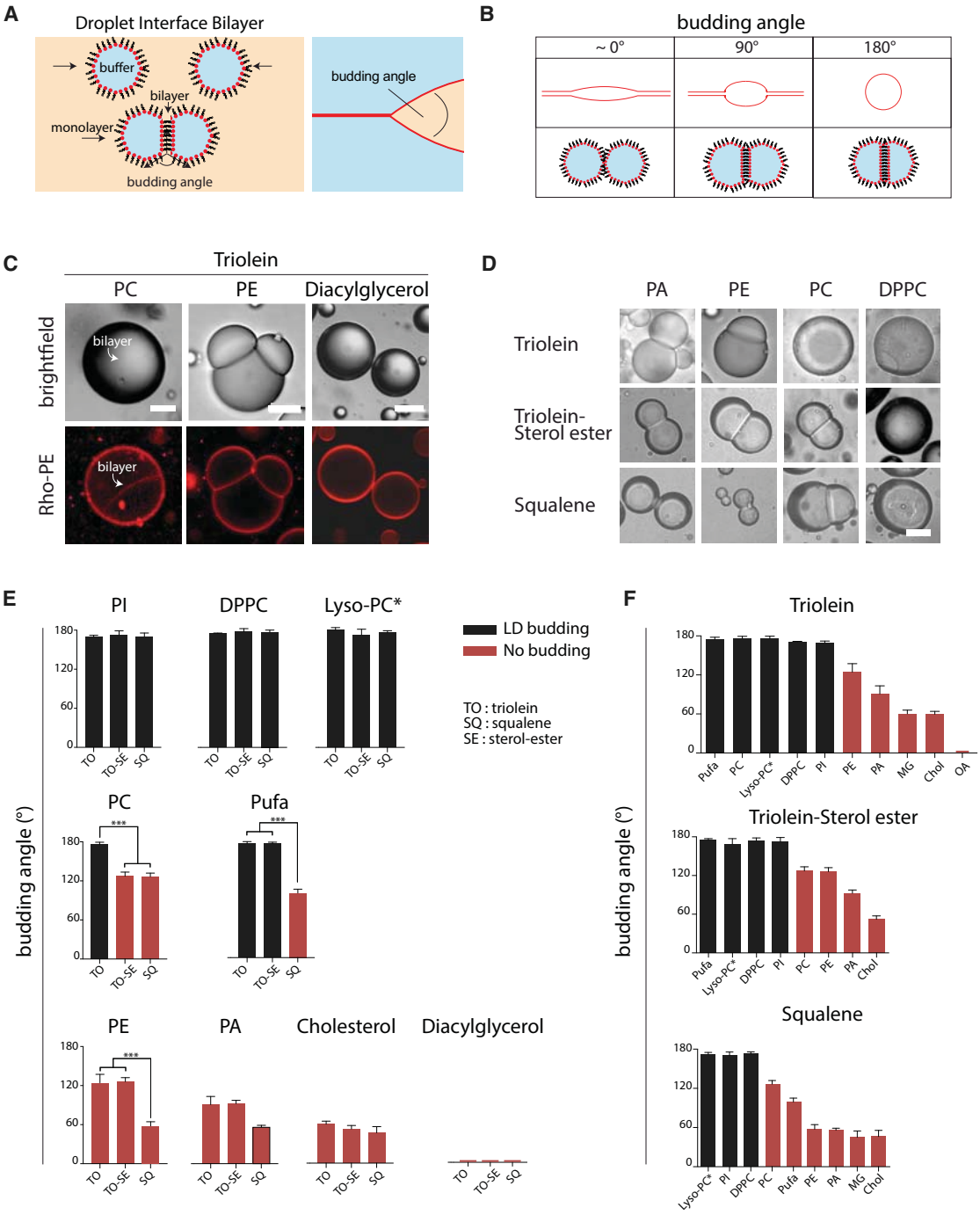

Figure 2. Determination of the Individual Contribution of Phospholipids on LD Budding

(A) Diagram of the principle of the droplet interface bilayer. Right diagram illustrates the analogy with an LD forming in the ER and the budding angle.

(B) Equivalence between the budding shape and the droplet interface bilayer, based on the budding angle.

(C) Example cases of droplet interface bilayers of different angles formed using triolein and phosphatidylcholine (PC), phosphatidylethanolamine (PE), and dioleoyl glycerol. Rhodamine-PE served as a marker for the monolayer and bilayer interfaces. Scale bars represent 10, 20, and 50 μm, respectively.

(D) Images of droplet interface bilayers made with other lipid compositions. Scale bar, 20 μm.

(E) Quantification of the budding angles for the lipid surfactants in the presence of different neutral lipids (red: non-budding compositions, the budding angle is below 180°; black: budding compositions, the budding angle is close to 180°). Lyso-PC* corresponds to a mixture of Lyso-PC and PA at a ratio of 20:80. More than 20 droplet interface bilayer angles were quantified for each composition. Error bars represent the SD. ***$p < 0.0001$.

(F) Representation of the budding angle for given neutral lipids and varied lipid surfactants. Error bars represent the SD.

See also Figure S2 and Movie S3.

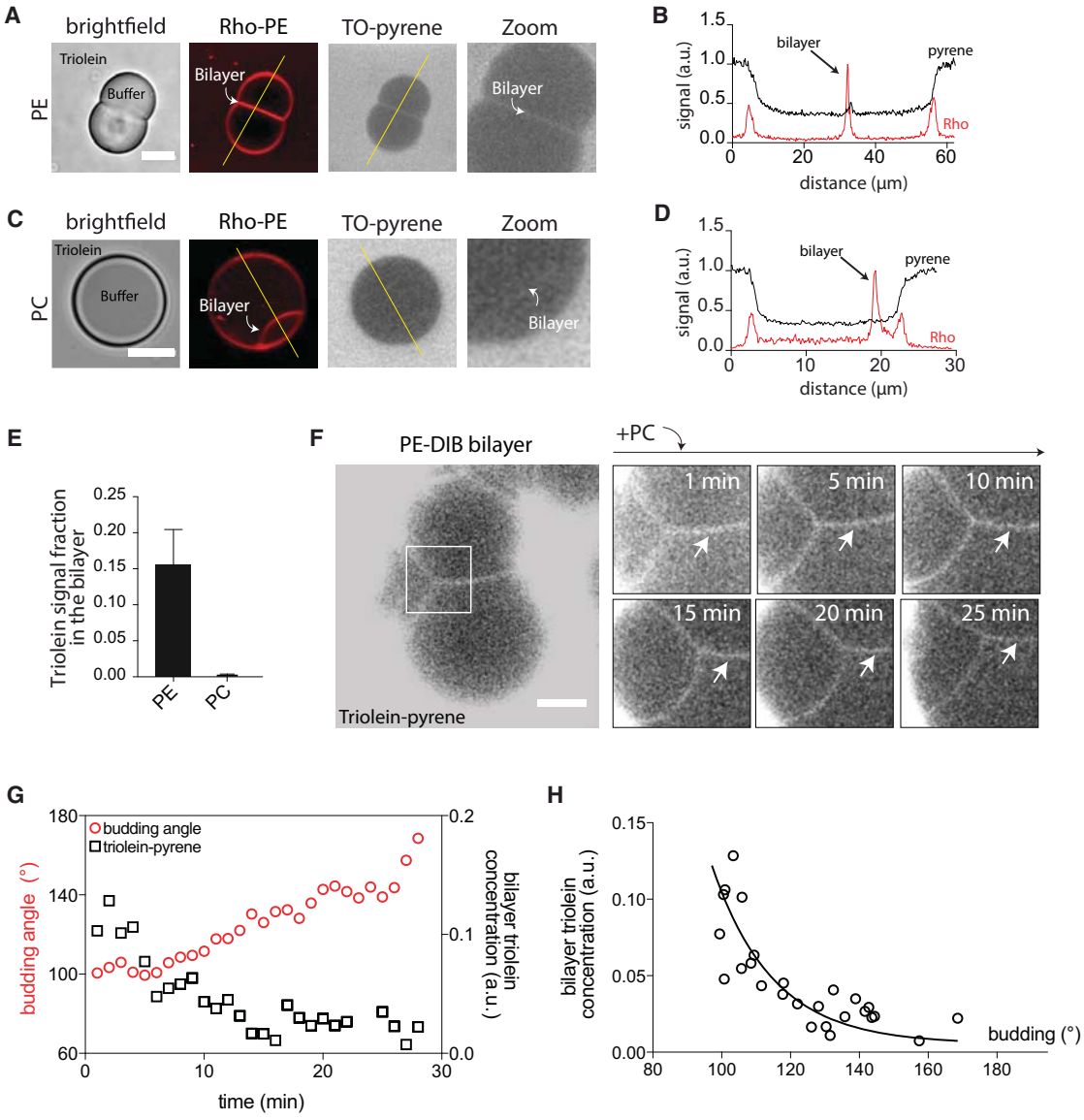

Figure 3. LD Budding Is Concomitant with the Natural Neutral Lipid Egress from the Bilayer

(A) Droplet interface bilayers made with PE in triolein containing 5% triolein-pyrene have the signal in the bilayer (blue signal and zoom). Scale bar, 10 μm.

(B) Rhodamine-PE, marking the bilayer and the monolayer, and triolein-pyrene, marking triolein localization, are plotted over the section made in (A).

(C and D) Almost no triolein signal is detected in PC-droplet interface bilayer. Scale bar, 20 μm.

(E) Concentration of triolein-pyrene in the bilayer compared with the surrounding bulk triolein phase (as in A–D). This concentration is about 15% for PE-droplet interface bilayer and almost 0 for PC-droplet interface bilayer. Error bars represent the SD.

(F) Addition of PC-in-triolein in the phase surrounding a PE-droplet interface bilayer leads over time to the removal of triolein-pyrene from the bilayer and the increase of the angle. The arrows point to the bilayer signal. Scale bar, 30 μm.

(G) Quantification of triolein-pyrene removal from the bilayer. The decrease of the triolein concentration is concomitant with the increase of the budding angle that marks the recruitment of PC to the droplet interface bilayer.

(H) Decrease rate of the triolein bilayer concentration with the budding angle.

See also Figure S3.

tension of the monolayer separating the cytosol and the LD, and the surface tension of the monolayer separating the LD and the ER lumen. The shape of a forming LD (Figure 4A), i.e., the budding angle, would arise from the competition between these tensions (Figure 4A) (Kusumaatmaja and Lipowsky, 2011; Lipowsky, 1993; Thiam and Foret, 2016): the bilayer tension pulls on the edge to flatten the LD (Figure 4A), while the monolayer tensions pull on the opposite direction to make the LD spherical.

In the droplet interface bilayer system, the two monolayers have the same tension γ_m and the bilayer tension is γ_b. The budding angle θ is related to the tensions by the Young equation $\gamma_b = 2\gamma_m \cos(\theta/2)$. For a given lipid composition, we can measure

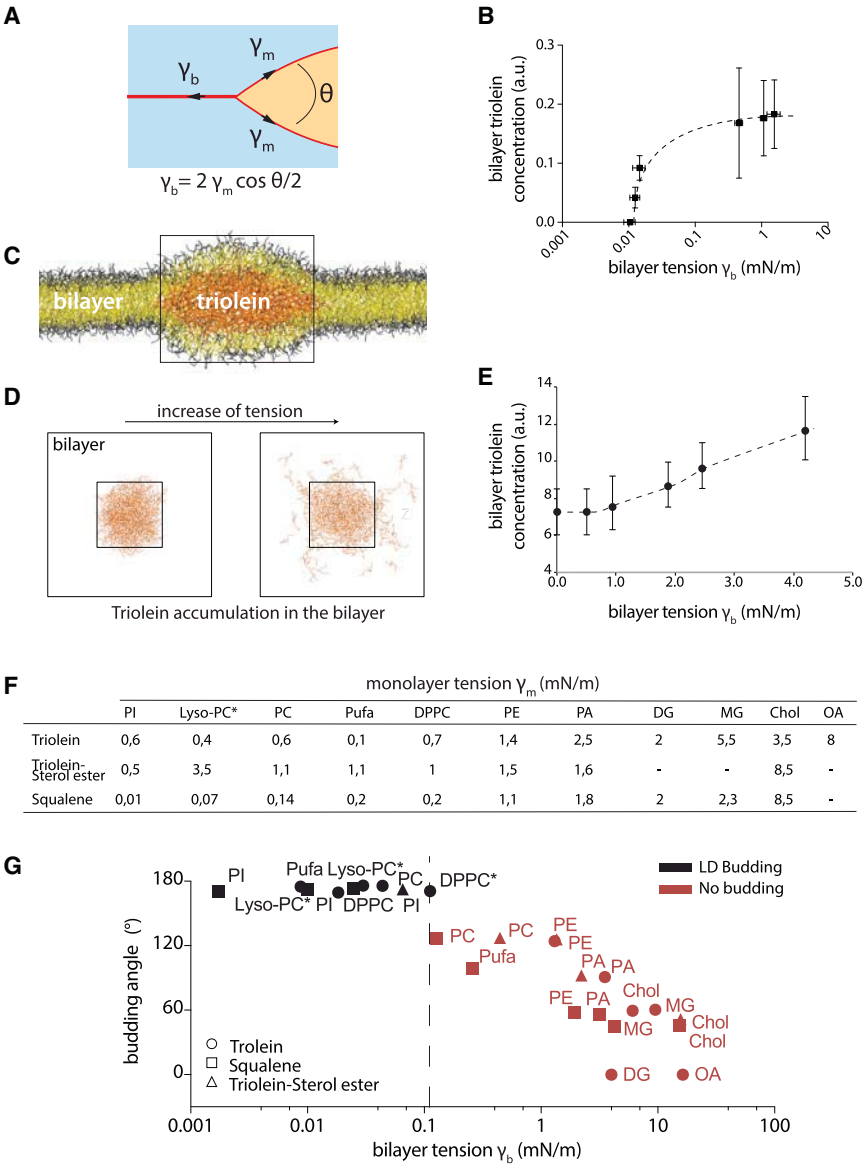

F

monolayer tension γ_m (mN/m)

	PI	Lyso-PC*	PC	Pufa	DPPC	PE	PA	DG	MG	Chol	OA
Triolein	0,6	0,4	0,6	0,1	0,7	1,4	2,5	2	5,5	3,5	8
Triolein-Sterol ester	0,5	3,5	1,1	1,1	1	1,5	1,6	-	-	8,5	-
Squalene	0,01	0,07	0,14	0,2	0,2	1,1	1,8	2	2,3	8,5	-

Figure 4. Surface Tension Controls the Neutral Lipid Egress from the Bilayer and LD Budding

(A) Diagram showing the different surface tensions acting on the neutral lipid phase. The balance between the different surface tensions defines the budding angle through the Young equation. The monolayer tension is γ_m and the bilayer tension is γ_b.

(B) The amount of triolein-pyrene in the droplet interface bilayer increases with the bilayer tension, which is varied by changing PC/PE ratios. Error bars represent the SD.

(C) Side view of the in silico model used to investigate the effect of a PC bilayer surface tension on the free triolein concentration in the bilayer.

(D) Top view of the in silico model in (C); only triolein molecules are shown. During the molecular dynamics simulations, triolein molecules escape the lens and relocate in the bilayer.

(E) Increasing the bilayer surface tension in silico increases the amount of free triolein molecules the bilayer. The fraction of triolein in the bilayer is compared with the amount of PC molecules in the bilayer. Error bars represent the SD.

(F) Monolayer surface tensions for the different lipid conditions probed for budding. Measurements were done by the pendant drop method. Lyso-PC* corresponds to a mixture of Lyso-PC with PA at a ratio of 20:80.

(G) Evolution of the droplet interface bilayer tension with the budding angle. Budding occurs only for lipid conditions leading to a bilayer surface tension below 0.1 mN/m. Lyso-PC* corresponds to a mixture of Lyso-PC with PA at a ratio of 20:80. DPPC* corresponds to a mixture of DPPC with PA at a ratio of 75:25.

See also Figure S4.

the surface tension of the monolayer interface by using the drop tensiometer method (Figure S4A), and determine the bilayer tension by using the previous equation.

We first investigated the relationship between the neutral lipids removal from the bilayer and surface tension. In a triolein-pyrene-rich environment, as in Figures 3A and 3C, we made PC/PE-droplet interface bilayers with controlled ratios between the two phospholipids. For each condition, we measured the surface tensions (Figures S4B and S4C) and determined the triolein intensity in the bilayer. We observed that the amount of triolein in the bilayer decreased with the bilayer tension (Figure 4B), as well as with the monolayer tension (Figure S4D).

With the previous experiment, the bilayer tension cannot be directly controlled. To further test the effect of tension on the accumulation of free triolein molecules in the bilayer, we performed molecular dynamics simulations. This approach enabled us to separately control the bilayer tension and triolein concentration. We generated a system composed of a tensionless PC bilayer bearing a lens of triolein molecules (Figures 4C and 4D). We then ran simulations at different values of the bilayer tension, while keeping the number of triolein and phospholipid molecules constant. We observed that triolein molecules escaped from the lens to relocate into the bilayer (bilayer region in Figures 4D and S4E). As observed experimentally (Figure 4B), the concentration of free triolein molecules in the bilayer decreased with the bilayer tension (Figure 4E).

All of these results support that decreasing membrane tension favors the egress of the neutral lipids from the bilayer and their transfer into forming LDs. Since this egress was concomitant with LD budding (Figure 3H), these results also support that lowering membrane tension should also promote LD budding.

We next probed the effect of tension on LD budding. For all lipid compositions studied in Figure 2, we measured the monolayer tension (Figure 4F) and determined the corresponding bilayer tension (see Figure 4A). We found a clear transition in budding with the bilayer surface tension (Figure 4G). Regardless of the phospholipid or neutral lipid composition, there is critical bilayer tension, ~0.1 mN/m, below which budding occurred

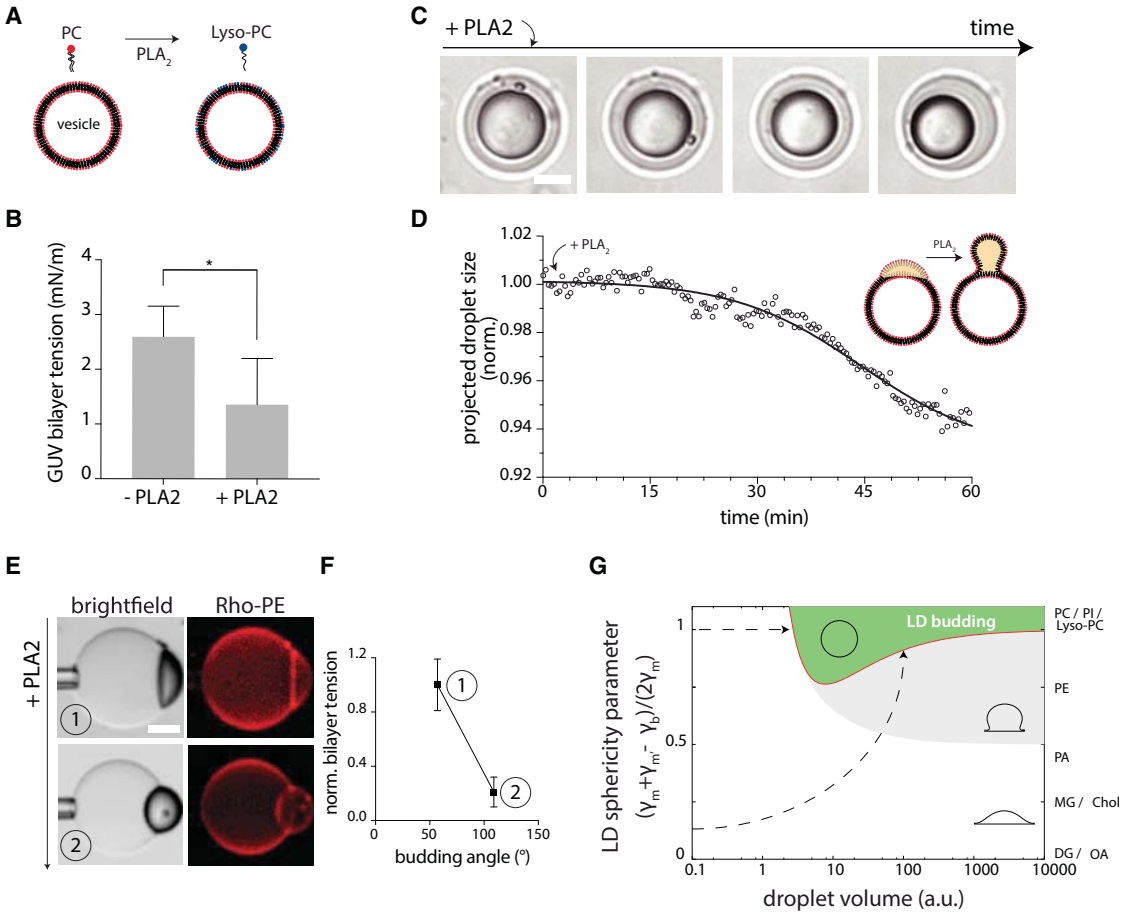

Figure 5. Phospholipase A_2 Activity Decreases the Bilayer Surface Tension and Induces Droplet Budding

(A) Conversion of PC to Lyso-PC by phospholipase A_2 (PLA_2).

(B) GUV bilayers submitted to PLA_2 action have a lower surface tension than control GUVs (n = 13). Error bars represent the SD. *$p < 0.01$.

(C) Top view of an artificial LD embedded in a GUV bilayer (the LD is on the apex of the GUV). The action of PLA_2 on the GUV membrane leads to the budding of the LD (n = 10). Scale bar, 10 μm.

(D) Evolution of the LD diameter over incubation time with PLA_2. The decrease of the diameter reveals the formation of a spherical LD.

(E) Side visualization of an artificial LD budding transition due to PLA_2 action. Scale bar, 10 μm.

(F) The GUV bilayer tension is measured before PLA_2 action (before budding, 1; after budding, 2). The bilayer tension is decreased by 5-fold. Error bars represent the SD.

(G) Illustrative phase diagram showing the LD budding region reached by altering membrane tensions (left axis) and/or phospholipid composition (right axis), considering a triolein neutral lipid phase. The LD sphericity parameter describes the competition between the different tensions for LD formation; it is defined as $(\gamma_m + \gamma_{m'} - \gamma_b)/(2\gamma_m)$.

See also Figure S5 and Movie S4.

(Figure 4G); a less clear transition occurred with the monolayer tension (Figure S4F). This result suggests that (1) decreasing the ER membrane surface tension promotes LD budding, and (2) phospholipids probably control LD budding by differently affecting membrane surface tension (Figure 4G).

Phospholipase A_2 Reduces the Bilayer Surface Tension and Induces LD Budding

Our previous results suggest that remodeling the ER phospholipid composition might control LD formation by regulating membrane surface tension (Figure 4G). We thus reasoned that phospholipid synthesis or remodeling enzymes would be important for LD formation. We decided to particularly focus on lyso-phospholipids that favored LD budding (Figure 2E). The presence of only 20% of Lyso-PC enabled the budding of LDs containing any of the neutral lipid tested (Figure 2E). In cells, lyso-phospholipid levels in the ER membrane depend in part on the activity of the cytosolic phospholipase A_2 (Penno et al., 2013; Pol et al., 2014). We therefore aimed to decipher in vitro the effect of phospholipase A_2 on LD budding.

We made GUVs containing PC/PA (70:30). A fraction of the GUVs was incubated with purified phospholipase A2 for 1 hr (Figure 5A). By using the microaspiration technique (Figure S1A), we determined the surface tension of the two GUV populations and found a lower surface tension for the population subjected to phospholipase A_2 (Figure 5B). Interestingly, the maximum amount of lyso-phospholipids generated by the phospholipase was around 15% of the total phospholipids (Figures S5A and S5B), which is close to lyso-phospholipid levels on LDs (~10%) and on bilayers (~20%) (Figure S5C) (Tauchi-Sato

et al., 2002). This observation suggests that the local production of few Lyso-PC molecules by phospholipase A_2 can decrease the ER bilayer tension.

We next made PC/PA (70:30) GUVs and incorporated artificial triolein LDs, which were in a non-budded state (Figure 5C). We added phospholipase A_2 into the surrounding aqueous phase and systematically observed budding events of the artificial LDs after few minutes (Figures 5C, 5D, and S5H; Movie S4), compared with controls (Figures S5D and S5E). This budding event was indeed associated with a decrease of the GUV bilayer tension (Figures 5E, 5F, S5F, and S5G). This experiment supports that phospholipase A_2 can decrease the ER surface tension to allow LD formation.

All presented data (Figures 4 and 5A–5F) emphasize the major contribution of surface tensions to LD budding. The action of phospholipase A_2 on LD budding illustrates only in part how cells can regulate tension by remodeling ER phospholipid composition. To have a broader and illustrative view of the possible mechanical and biochemical regulatory pathways of LD formation, we built a simplified physical model. This model assumes that an LD deforms only toward the cytosolic side (Figure S5I and STAR Methods). We computed a phase diagram (Figure 5G) showing the relative values of tensions (included in the sphericity parameter of Figure 5G), and volumes, for which an LD buds off. We observed as expected that the LD shape is mainly dictated by the tensions (except at very small sizes, STAR Methods), and budding is obtained by lowering the bilayer surface tension (Figure 5G, left axis). During the LD growth until budding, different regulatory pathways of phospholipids (Figure 5G, right axis) and/or tensions (Figure 5G, left axis) could enable reaching the budding region at different LD formation sizes (Figure 5G, arrows).

Targeted Phospholipid Alteration in Cells Leads to Anticipated LD Size Variation

We wanted to further test in cells our in vitro findings by modulating LD formation. Directly controlling the ER membrane tension is experimentally challenging. We thus decided to modulate phospholipid composition. However, directly imaging the structural shape changes of forming LDs is not easy. Instead, from the differential budding aptitudes of phospholipids (Figures 2 and 3), we can predict LD size variation and phenotype (Figure 6A): budding conditions favor the formation of small LDs; non-budding conditions favor the formation of large LDs that remain connected to the ER membrane, and the accumulation of neutral lipids in the ER membrane.

Before testing our predictions, we first scanned the literature and selected studies where LD size distribution varied (Figure S6A). Most of these studies focused on the function of proteins whose alteration affected LD formation. However, the alteration of the proteins was often associated with important changes on the cellular lipidome (Figure S6A), which might be actually a key reason for the observed LD phenotype (Figure 6A).

To next test our predictions, we first focused on Lyso-PC, which favored budding (Figures 5C–5F) and is normally present in cells at relatively low levels compared with PC. We reasoned that blocking the acylation of Lyso-PC by inhibiting the lysophosphatidylcholine acyltransferase 1 (LPCAT1) (Figure 6B) would increase Lyso-PC levels and favor the formation of small LDs (Figure 6A). We instead observed that LDs were a little larger than in control cells (Figures S6F–S6H) as previously reported (Moessinger et al., 2011). However, Lyso-PC is recycled into Lyso-PA and then to PA, ensuing the action of the plasma secreted lyso-phospholipase D, autotaxin (Figure 6B). We thus conducted concomitant small interfering RNA (siRNA) of LPCAT1 and the pharmacological inhibition of autotaxin. Under this condition, we found that LDs became indeed smaller than in control cells (Figures 6C–6E), and their size was autotaxin inhibitor dose-dependent (Figure S6I).

Second, we found that phospholipases affected LD formation size (Figures 6F–6H and S6J–S6L, and data not shown). The deletion of the cytosolic phospholipase A_2 by siRNA in various cellular types depletes lyso-phospholipids and leads to the accumulation of neutral lipids in the ER (Gubern et al., 2008); LDs do not efficiently bud in this context as we predicted (Figure 6A). Instead of the siRNA approach, we decided to decrease lyso-phospholipid levels by treating HeLa and Huh7 cells with the cytosolic phospholipase A_2 inhibitor methyl arachidonyl fluorophosphonate (Gubern et al., 2008). We observed, as predicted, the occurrence of bigger LDs than in control cells (Figures 6F–6H). We finally probed the opposite case with the overexpression of the cytosolic phospholipase A_2 in HeLa and Huh7 cells. After 24 hr of overexpression, we induced LD formation by oleate loading and determined LD size distribution after 4 hr. We observed, as expected, that LDs were smaller than in control cells (Figures 6F–6H).

Third, we focused on saturated phospholipids that efficiently budded LDs in vitro (Figure 2E). Accumulation of saturated phospholipids should promote the formation of small LDs (Figure 6A). We confirmed this prediction in different cell types. For example, we pharmacologically inhibited stearoyl-coenzyme A desaturase 1 (SCD1) in Huh7 cells for 24 hr to promote the accumulation of saturated phospholipids. We then oleate loaded the cells and observed that LDs were significantly smaller than in control cells (Figures 6I–6K).

Finally, we studied the accumulation of squalene, as it appeared to be the most difficult neutral lipid to package into spherical LDs (Figure 2F). We predicted that increased squalene levels in cells should favor the formation of large LDs (Figure 6A). HeLa cells devoid of LDs were cultured in the presence of mevalonic acid, a precursor of squalene that further is transformed into sterol ester (Figure 6L). We detected by thin-layer chromatography the synthesis of sterol esters (Figure S6M). These cells were considered as control cells and their LD size was measured 4 hr after mevalonic acid loading. We next pretreated the cells with terbinafine, which blocked the squalene epoxidase and favored squalene deposition (Figures 6L and S6M). We observed, as predicted, the formation of numerous and bigger LDs compared with control cells (Figures 6M–6O). Finally, we repeated the same experiment but with inhibition of SCD1 for 24 hr, prior to terbinafine treatment and mevalonic acid loading. This strategy was adopted to favor the accumulation of saturated phospholipids that should facilitate the budding of smaller squalene-containing LDs (Figures 2E and 6A). As anticipated, we detected that the additional SCD1 inhibition shifted LD size toward smaller ones (Figures 6M–6O).

These experiments with cells matched our predictions and support the conclusion that ER phospholipids control LD formation, possibly by modulating ER membrane tension. Differences

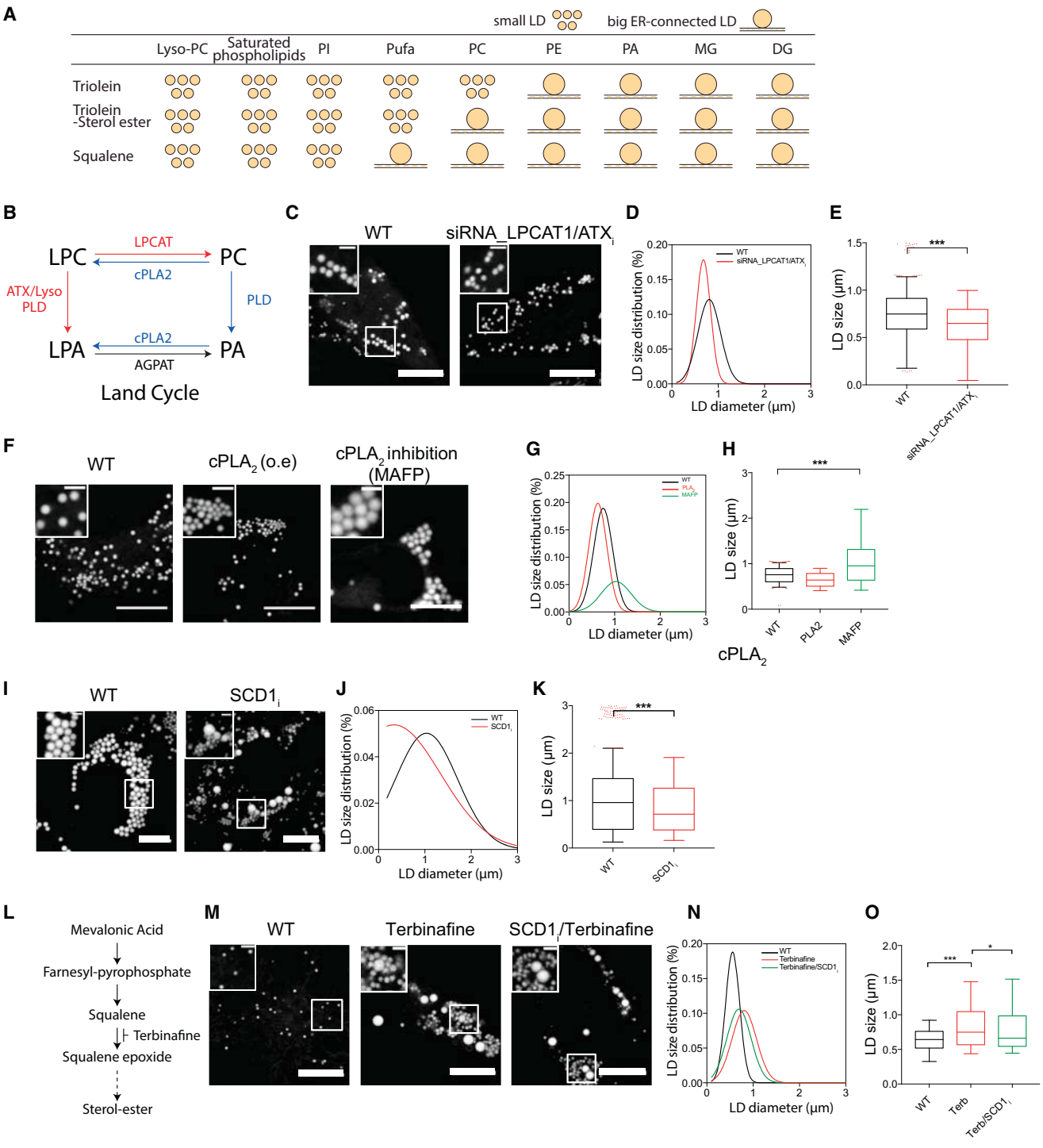

Figure 6. Targeted Alteration of Cellular Lipid Composition Modulates LD Formation Size in a Predictable Manner

(A) Predicted phenotypes for different lipid compositions. Budding conditions are predicted to mediate the formation of small LDs. Non-budding conditions are predicted to mediate the formation of big LDs connected with the ER, and to potentially mediate the accumulation of neutral lipids in the ER bilayer.

(B) Phospholipid biosynthesis pathways in the Land cycle.

(C–E) In HeLa cells, the double inhibition of LPCAT1, by siRNA, and ATX/Lyso-phospholipase D, by an autotaxin inhibitor, ATXi (C), favors the formation of smaller LDs than in wild-type (WT) (D and E). Scale bars, 10 µm. ***$p < 0.0001$.

(F–H) The overexpression of c-PLA$_2$ in HeLa cells decreases LD size distribution, after 4 hr oleate loading, as compared with WT (F). Inhibition of the PLA$_2$ by the methyl arachidonyl fluorophosphonate (MAFP) increases LD size distribution under the same conditions (G and H). ***$p < 0.0001$. Scale bars, 10 µm.

(I–K) The pharmacological inhibition of SCD1 in Huh7 cells (I) leads to a significant shift of LD size to smaller ones (J and K). Scale bars, 10 µm. ***$p < 0.0001$.

(legend continued on next page)

in ER phospholipid compositions, e.g., between cell lines or types, likely underlie differences in LD formation size.

DISCUSSION

We have investigated how LDs form from the ER, one of the most important questions of LD biology. We have uncovered in detail that ER phospholipids and surface tension determine LD formation. The LD formation size is determined by these chemical and physical parameters of the ER. Mechanistically, phospholipids affect the ER membrane surface tension whose decrease favors the egress of neutral lipids from the bilayer and their packaging into spherical LDs. Our discovery constitutes a major step in understanding LD biogenesis and regulation. We have highlighted the importance of possible alterations of ER phospholipids and tension on LD regulation. The action of proteins on LD regulation can now be better probed, and understood, by knowing their impact on these chemical and physical aspects of the ER membrane.

We have found in vitro that PC alone promoted the budding of triglyceride but not of sterol ester LDs. On the contrary, PI or saturated phospholipids promoted the budding of all tested neutral lipids (Figure 2E). Therefore, whenever the ratio between neutral lipids is affected in cells, e.g., due to metabolic shifts, a concomitant alteration of the membrane phospholipid composition in PC and PI, for example, could occur to enable LD formation.

In some biological cases, synthesized neutral lipids fail to integrate LDs and stay in the ER. This is the case, for example, of squalene in yeast cells (Spanova et al., 2010), which is probably due to the poor ability of PC, the major ER phospholipid, to bud pure squalene LDs (Figure 2E). In this condition, increasing triglyceride levels facilitates squalene incorporation into LDs (Spanova et al., 2010). Alternatively, squalene can be packaged into LDs by increasing the saturation degree of phospholipids (Figures 2E and 6M–6O).

Saturated phospholipids are usually in the ER at low concentrations because of their role in ER stress. However, their level is increased under lipotoxic conditions to alleviate cells from lipotoxicity, through facilitating LD formation (Iwai et al., 2016). This effect on LD formation is consistent with our finding that saturated phospholipids efficiently package neutral lipids into LDs (Figures 2E and 6M–6O). Furthermore, the presence of saturated phospholipids in the ER depends on the activity of the desaturase enzyme SCD1. When SCD1 is defective the saturation of ER phospholipids increases, which favors the formation of very small LDs (Figures 6A and 6I–6K). This phenotype has been consistently observed in *Caenorhabditis elegans* with defective SCD1 (Shi et al., 2013), or in adipose tissues wherein Seipin dysfunction impaired SCD1 activity (Boutet et al., 2009; Lounis et al., 2016).

There are other examples illustrating the importance of phospholipids on LD budding. For example, triglycerides accumulate in the ER in the dysfunction of Lipin, which converts PA into diacylglycerols (Adeyo et al., 2011). This phenotype is consistent with the inefficiency of LD budding in PA accumulation (Figure 2E) and, more generally, with the accumulation of free neutral lipids in the bilayer under non-budding conditions (Figures 3A, 3B, and 6A). Another example, which is extreme, is the formation of lipoprotein particles, which are particular forms of LDs made in the ER lumen. The budding of triglyceride-containing lipoproteins requires the local production of polyunsaturated phospholipids by LPCAT3 (Hashidate-Yoshida et al., 2015). We have found that these phospholipids specially allowed the budding of triglyceride droplets (Figure 2E).

Instead of a dynamic alteration of phospholipids or surface tension for LD budding, the ER may simply display regions or microdomains (Kassan et al., 2013) enriched with particular phospholipids or that transiently have specific surface tensions. Such segregation could occur between the smooth and rough ER, nuclear and peripheral ER, and ER tubules and sheets (Lagace and Ridgway, 2013). These differences could allow the formation of distinct pools of LDs containing different lipids and proteins and having different sizes (Thiam and Beller, 2017). This could explain the occurrence in various cell types of separated sterol ester and triglyceride LDs, distinctly marked by different perilipin proteins (Hsieh et al., 2012; Meyers et al., 2016), or the existence of metabolically distinct diacylglycerol transferase 1- and 2-LDs, which have different sizes (Wilfling et al., 2013).

Variation of LD size is often observed between cell lines or types, or is due to the dysfunction of some proteins (Thiam and Beller, 2017). The origin of such variability remains very unclear except for very specific cases where LDs split, fuse, or grow (Gong et al., 2011; Long et al., 2012; Tan et al., 2014; Wilfling et al., 2013; Yang et al., 2012). Our results support that LDs can simply form at different sizes as a result of differences in the ER phospholipid composition and/or tension (Figures 5G and 6A). For example, the deletion of proteins such as Rab, Atlastin, Reticulon, or Torsin, which do not necessarily affect ER phospholipids but morphology or shape, modulate LD size probably through modulating ER surface tension (Grillet et al., 2016; Klemm et al., 2013; Zerial and McBride, 2001). Indeed, mechanical pulling on the ER membrane increases tension, works against budding, and increases LD formation size.

Finally, many proteins important for LD functionality target LDs from the ER, either during LD formation or via ER-LD connection bridges (Jacquier et al., 2011; Wilfling et al., 2013, 2014a, 2014b). These proteins encompass the glycerol-3-phosphate acyltransferase enzyme (GPAT4) (Wilfling et al., 2013) that localizes to LD surface to mediate the local synthesis of neutral lipids. Our results suggest that non-budding conditions favor ER-LD connection (Figure 6A), and should enhance the trafficking of proteins between ER and LD. These conditions correspond, for example, to the accumulation of negatively curved lipids such as diacylglycerols, PA, or cholesterol (Figure 1G), which had higher surface

(L) Terbinafine blocks squalene epoxidation that is necessary for the biosynthesis of sterol esters.
(M–O) HeLa cells cultured in the presence of mevalonic acid form LDs whose size is considered WT size. Treatment of the cells with terbinafine prior to mevalonic acid loading (M) induces squalene deposition and promotes the formation of bigger LDs than in WT cells. Inhibition of SCD1, prior terbinafine treatment, and mevalonic loading lead to the formation of LDs smaller than in the single terbinafine treatment (N and O). Scale bars, 10 μm. ***$p < 0.0001$, *$p < 0.01$.
See also Figure S6.

tensions (Figure 4G). Our prediction is consistent with reported regulations of GPAT4 trafficking from ER to LDs: in increased PA levels in the ER membrane of various cell types lacking Seipin protein, a massive transfer of GPAT4 from the ER to almost all LDs is observed in comparison with normal cells (Fei et al., 2011; Pagac et al., 2016; Szymanski et al., 2007; Wang et al., 2016); likewise, under conditions where GPAT4 should exclusively remain in the ER membrane of fly cells (Wilfling et al., 2014b), the induction of cholesterol accumulation in the membrane restored GPAT4 targeting from ER to LDs (Wilfling et al., 2014b). Consequently, ER tension and phospholipid composition seem to be critical for determining the protein composition of LD during formation.

In summary, we have unveiled ER lipid composition and membrane tension as key parameters of LD formation. Our discovery brings major insights on how proteins could regulate LDs. In particular, by locally altering ER phospholipid composition or surface tension, proteins might determine where LDs form and which, and how, proteins target LD surface.

STAR★METHODS

Detailed methods are provided in the online version of this paper and include the following:

- KEY RESOURCES TABLE
- CONTACT FOR REAGENT AND RESOURCE SHARING
- METHOD DETAILS
  - Droplet Interface Bilayer Formation
  - Preparation of the Oil Phase
  - Droplet Interface Bilayer Angle and Bilayer Triolein Signal Determinations
  - Giant Unilamellar Vesicles and Artificial Lipid Droplets Formation
  - Measurement of the Interfacial Tension of the Interface of Artificial Droplets
  - Surface Tension Measurements by Microaspiration
  - Cellular Fractionation
  - Lipid Extraction
  - Thin Layer Chromatography and Lipid Detection
  - Cellular Lipid Droplet Size Measurements
  - Cell Culture
  - Overexpression of Phospholipase A2
  - Enzymes Inhibitions
  - Induction of Squalene Accumulation
  - Relevance of Curvature for Lipid Droplet Budding (Related to Figures 1 and 2)
  - Theoretical Modeling of the Shape of Lipid Droplet Budding (Related to Figure 5G)
  - Molecular Dynamics (MD) Simulations (Related to Figures 4C–4E)
- QUANTIFICATION AND STATISTICAL ANALYSIS
- DATA AND SOFTWARE AVAILABILITY

SUPPLEMENTAL INFORMATION

Supplemental Information includes six figures and four movies

AUTHOR CONTRIBUTIONS

A.R.T. conceived the project. K.B.M., D.A., A.C., and A.R.T. conducted experiments. L.F. established the mathematical modeling. S.V performed molecular dynamics simulations. K.B.M., D.A., A.C., S.V., L.F., and A.R.T analyzed data. A.R.T. wrote the manuscript with feedback from co-authors K.B.M., S.V., and L.F.

ACKNOWLEDGMENTS

We thank Drs. Frederic Pincet, Philippe Rostaing, Catherine Cantrel, Alain Cagna from Teclis Company, and Simon Kulifaj for technical assistance and helpful discussions. We thank the members of the group for comments and critical discussions. This work was supported by the ATIP-Avenir program and Programme Emergence de la Ville de Paris to A.R.T., the ANRS Agence Autonome de l'Inserm (ECTZ7095, ECTZ20454) to A.R.T. and D.A, and ANR-16-TERC-0002-01.

REFERENCES

Adeyo, O., Horn, P.J., Lee, S., Binns, D.D., Chandrahas, A., Chapman, K.D., and Goodman, J.M. (2011). The yeast lipin orthologue Pah1p is important for biogenesis of lipid droplets. J. Cell Biol. *192*, 1043–1055.

Bacle, A., Gautier, R., Jackson, C.L., Fuchs, P.F.J., and Vanni, S. (2017). Interdigitation between Triglycerides and Lipids Modulates Surface Properties of Lipid Droplets. Biophys. J. *112*, 1417–1430.

Bayley, H., Cronin, B., Heron, A., Holden, M.A., Hwang, W.L., Syeda, R., Thompson, J., and Wallace, M. (2008). Droplet interface bilayers. Mol. Biosyst. *4*, 1191–1208.

Boutet, E., El Mourabit, H., Prot, M., Nemani, M., Khallouf, E., Colard, O., Maurice, M., Durand-Schneider, A.M., Chretien, Y., Gres, S., et al. (2009). Seipin deficiency alters fatty acid Delta 9 desaturation and lipid droplet formation in Berardinelli-Seip congenital lipodystrophy. Biochimie *91*, 796–803.

Cartwright, B.R., Binns, D.D., Hilton, C.L., Han, S., Gao, Q., and Goodman, J.M. (2015). Seipin performs dissectible functions in promoting lipid droplet biogenesis and regulating droplet morphology. Mol. Biol. Cell *26*, 726–739.

Chernomordik, L.V., and Kozlov, M.M. (2003). Protein-lipid interplay in fusion and fission of biological membranes. Annu. Rev. Biochem. *72*, 175–207.

Choudhary, V., Ojha, N., Golden, A., and Prinz, W.A. (2015). A conserved family of proteins facilitates nascent lipid droplet budding from the ER. J. Cell Biol. *211*, 261–271.

Ding, W., Palaiokostas, M., Wang, W., and Orsi, M. (2015). Effects of lipid composition on bilayer membranes quantified by all-atom molecular dynamics. J. Phys. Chem. B *119*, 15263–15274.

Fei, W., Shui, G., Zhang, Y., Krahmer, N., Ferguson, C., Kapterian, T.S., Lin, R.C., Dawes, I.W., Brown, A.J., Li, P., et al. (2011). A role for phosphatidic acid in the formation of "supersized" lipid droplets. PLoS Genet. *7*, e1002201.

Foret, L. (2014). Shape and energy of a membrane bud induced by protein coats or viral protein assembly. Eur. Phys. J. E Soft Matter *37*, 42.

Gong, J., Sun, Z., Wu, L., Xu, W., Schieber, N., Xu, D., Shui, G., Yang, H., Parton, R.G., and Li, P. (2011). Fsp27 promotes lipid droplet growth by lipid exchange and transfer at lipid droplet contact sites. J. Cell Biol. *195*, 953–963.

Grillet, M., Dominguez Gonzalez, B., Sicart, A., Pottler, M., Cascalho, A., Billion, K., Hernandez Diaz, S., Swerts, J., Naismith, T.V., Gounko, N.V., et al. (2016). Torsins are essential regulators of cellular lipid metabolism. Dev. Cell *38*, 235–247.

Gubern, A., Casas, J., Barcelo-Torns, M., Barneda, D., de la Rosa, X., Masgrau, R., Picatoste, F., Balsinde, J., Balboa, M.A., and Claro, E. (2008). Group IVA phospholipase A2 is necessary for the biogenesis of lipid droplets. J. Biol. Chem. *283*, 27369–27382.

Guo, Y., Walther, T.C., Rao, M., Stuurman, N., Goshima, G., Terayama, K., Wong, J.S., Vale, R.D., Walter, P., and Farese, R.V. (2008). Functional genomic screen reveals genes involved in lipid-droplet formation and utilization. Nature *453*, 657–661.

Guo, Y., Cordes, K.R., Farese, R.V., Jr., and Walther, T.C. (2009). Lipid droplets at a glance. J. Cell Sci. *122*, 749–752.

Hashidate-Yoshida, T., Harayama, T., Hishikawa, D., Morimoto, R., Hamano, F., Tokuoka, S.M., Eto, M., Tamura-Nakano, M., Yanobu-Takanashi, R., and Mukumoto, Y. (2015). Fatty acid remodeling by LPCAT3 enriches arachidonate in phospholipid membranes and regulates triglyceride transport. Elife *4*, e06328.

Hsieh, K., Lee, Y.K., Londos, C., Raaka, B.M., Dalen, K.T., and Kimmel, A.R. (2012). Perilipin family members preferentially sequester to either triacylglycerol-specific or cholesteryl-ester-specific intracellular lipid storage droplets. J. Cell Sci. *125*, 4067–4076.

Humphrey, W., Dalke, A., and Schulten, K. (1996). VMD: visual molecular dynamics. J. Mol. Graph. *14*, 33–38.

Iwai, T., Kume, S., Chin-Kanasaki, M., Kuwagata, S., Araki, H., Takeda, N., Sugaya, T., Uzu, T., Maegawa, H., and Araki, S.I. (2016). Stearoyl-CoA desaturase-1 protects cells against lipotoxicity-mediated apoptosis in proximal tubular cells. Int. J. Mol. Sci. *17*, E1868.

Jacquier, N., Choudhary, V., Mari, M., Toulmay, A., Reggiori, F., and Schneiter, R. (2011). Lipid droplets are functionally connected to the endoplasmic reticulum in *Saccharomyces cerevisiae*. J. Cell Sci. *124*, 2424–2437.

Julicher, F., and Seifert, U. (1994). Shape equations for axisymmetrical vesicles—a clarification. Phys. Rev. E Stat. Phys. Plasmas Fluids Relat. Interdiscip. Topics *49*, 4728–4731.

Kabalnov, A., and Wennerström, H. (1996). Macroemulsion stability: the oriented wedge theory revisited. Langmuir *12*, 276–292.

Kadereit, B., Kumar, P., Wang, W.J., Miranda, D., Snapp, E.L., Severina, N., Torregroza, I., Evans, T., and Silver, D.L. (2008). Evolutionarily conserved gene family important for fat storage. Proc. Natl. Acad. Sci. USA *105*, 94–99.

Kassan, A., Herms, A., Fernandez-Vidal, A., Bosch, M., Schieber, N.L., Reddy, B.J., Fajardo, A., Gelabert-Baldrich, M., Tebar, F., Enrich, C., et al. (2013). Acyl-CoA synthetase 3 promotes lipid droplet biogenesis in ER microdomains. J. Cell Biol. *203*, 985–1001.

Klemm, R.W., Norton, J.P., Cole, R.A., Li, C.S., Park, S.H., Crane, M.M., Li, L., Jin, D., Boye-Doe, A., Liu, T.Y., et al. (2013). A conserved role for atlastin GTPases in regulating lipid droplet size. Cell Rep. *3*, 1465–1475.

Kusumaatmaja, H., and Lipowsky, R. (2011). Droplet-induced budding transitions of membranes. R. Soc. Chem. *7*, 6914–6919.

Lagace, T.A., and Ridgway, N.D. (2013). The role of phospholipids in the biological activity and structure of the endoplasmic reticulum. Biochim. Biophys. Acta *1833*, 2499–2510.

Lipowsky, R. (1993). Domain-induced budding of fluid membranes. Biophys. J. *64*, 1133–1138.

Long, A.P., Manneschmidt, A.K., VerBrugge, B., Dortch, M.R., Minkin, S.C., Prater, K.E., Biggerstaff, J.P., Dunlap, J.R., and Dalhaimer, P. (2012). Lipid droplet de novo formation and fission are linked to the cell cycle in fission yeast. Traffic *13*, 705–714.

Lounis, M.A., Lalonde, S., Rial, S.A., Bergeron, K.F., Ralston, J.C., Mutch, D.M., and Mounier, C. (2016). Hepatic BSCL2 (Seipin) deficiency disrupts lipid droplet homeostasis and increases lipid metabolism via SCD1 activity. Lipids *52*, 129–150.

Martin, S., and Parton, R.G. (2006). Lipid droplets: a unified view of a dynamic organelle. Nat. Rev. Mol. Cell Biol. *7*, 373–378.

Meyers, A., Del Rio, Z.P., Beaver, R.A., Morris, R.M., Weiskittel, T.M., Alshibli, A.K., Mannik, J., Morrell-Falvey, J., and Dalhaimer, P. (2016). Lipid droplets form from distinct regions of the cell in the fission yeast *Schizosaccharomyces pombe*. Traffic *17*, 657–669.

Moessinger, C., Kuerschner, L., Spandl, J., Shevchenko, A., and Thiele, C. (2011). Human lysophosphatidylcholine acyltransferases 1 and 2 are located in lipid droplets where they catalyze the formation of phosphatidylcholine. J. Biol. Chem. *286*, 21330–21339.

Ohsaki, Y., Suzuki, M., and Fujimoto, T. (2014). Open questions in lipid droplet biology. Chem. Biol. *21*, 86–96.

Pagac, M., Cooper, D.E., Qi, Y., Lukmantara, I.E., Mak, H.Y., Wu, Z., Tian, Y., Liu, Z., Lei, M., and Du, X. (2016). SEIPIN regulates lipid droplet expansion and adipocyte development by modulating the activity of glycerol-3-phosphate acyltransferase. Cell Rep. *17*, 1546–1559.

Penno, A., Hackenbroich, G., and Thiele, C. (2013). Phospholipids and lipid droplets. Biochim. Biophys. Acta *1831*, 589–594.

Pol, A., Gross, S.P., and Parton, R.G. (2014). Review: biogenesis of the multifunctional lipid droplet: lipids, proteins, and sites. J. Cell Biol. *204*, 635–646.

Poulin, P., and Bibette, J. (1998). Adhesion of water droplets in organic solvent. Langmuir *14*, 6341–6343.

Saleem, M., Morlot, S., Hohendahl, A., Manzi, J., Lenz, M., and Roux, A. (2015). A balance between membrane elasticity and polymerization energy sets the shape of spherical clathrin coats. Nat. Commun. *6*, 6249.

Seifert, U., Berndl, K., and Lipowsky, R. (1991). Shape transformations of vesicles—phase-diagram for spontaneous-curvature and bilayer-coupling models. Phys. Rev. A *44*, 1182–1202.

Shi, X., Li, J., Zou, X.J., Greggain, J., Rodkaer, S.V., Faergeman, N.J., Liang, B., and Watts, J.L. (2013). Regulation of lipid droplet size and phospholipid composition by stearoyl-CoA desaturase. J. Lipid Res. *54*, 2504–2514.

Shinoda, W., DeVane, R., and Klein, M.L. (2007). Multi-property fitting and parameterization of a coarse grained model for aqueous surfactants. Mol. Simulation *33*, 27–36.

Spanova, M., Czabany, T., Zellnig, G., Leitner, E., Hapala, I., and Daum, G. (2010). Effect of lipid particle biogenesis on the subcellular distribution of squalene in the yeast *Saccharomyces cerevisiae*. J. Biol. Chem. *285*, 6127–6133.

Szymanski, K.M., Binns, D., Bartz, R., Grishin, N.V., Li, W.P., Agarwal, A.K., Garg, A., Anderson, R.G.W., and Goodman, J.M. (2007). The lipodystrophy protein seipin is found at endoplasmic reticulum lipid droplet junctions and is important for droplet morphology. Proc. Natl. Acad. Sci. USA *104*, 20890–20895.

Tan, J.S.Y., Seow, C.J.P., Goh, V.J., and Silver, D.L. (2014). Recent advances in understanding proteins involved in lipid droplet formation, growth and fusion. J. Genet. Genomics *41*, 251–259.

Tauchi-Sato, K., Ozeki, S., Houjou, T., Taguchi, R., and Fujimoto, T. (2002). The surface of lipid droplets is a phospholipid monolayer with a unique fatty acid composition. J. Biol. Chem. *277*, 44507–44512.

Thiam, A.R., and Beller, M. (2017). The why, when and how of lipid droplet diversity. J. Cell Sci. *130*, 315–324.

Thiam, A.R., and Foret, L. (2016). The physics of lipid droplet nucleation, growth and budding. Biochim. Biophys. Acta *1861*, 715–722.

Thiam, A.R., and Pincet, F. (2015). The energy of COPI for budding membranes. PLoS One *10*, e0133757.

Thiam, A.R., Bremond, N., and Bibette, J. (2011). Adhesive emulsion bilayers under an electric field: from unzipping to fusion. Phys. Rev. Lett. *107*, 068301.

Thiam, A.R., Bremond, N., and Bibette, J. (2012). From stability to permeability of adhesive emulsion bilayers. Langmuir *28*, 6291–6298.

Thiam, A.R., Antonny, B., Wang, J., Delacotte, J., Wilfling, F., Walther, T.C., Beck, R., Rothman, J.E., and Pincet, F. (2013a). COPI buds 60-nm lipid droplets from reconstituted water-phospholipid-triacylglyceride interfaces, suggesting a tension clamp function. Proc. Natl. Acad. Sci. USA *110*, 13244–13249.

Thiam, A.R., Farese, R.V., Jr., and Walther, T.C. (2013b). The biophysics and cell biology of lipid droplets. Nat. Rev. Mol. Cell Biol. *14*, 775–786.

Walther, T.C., and Farese, R.V., Jr. (2012). Lipid droplets and cellular lipid metabolism. Annu. Rev. Biochem. *81*, 687–714.

Wang, H., Becuwe, M., Housden, B.E., Chitraju, C., Porras, A.J., Graham, M.M., Liu, X.N., Thiam, A.R., Savage, D.B., Agarwal, A.K., et al. (2016). Seipin is required for converting nascent to mature lipid droplets. Elife *5*, e16582.

Welte, M.A. (2015). Expanding roles for lipid droplets. Curr. Biol. *25*, R470–R481.

Wilfling, F., Wang, H., Haas, J.T., Krahmer, N., Gould, T.J., Uchida, A., Cheng, J.X., Graham, M., Christiano, R., Frohlich, F., et al. (2013). Triacylglycerol synthesis enzymes mediate lipid droplet growth by relocalizing from the ER to lipid droplets. Dev. Cell *24*, 384–399.

Wilfling, F., Haas, J.T., Walther, T.C., and Farese, R.V., Jr. (2014a). Lipid droplet biogenesis. Curr. Opin. Cell Biol. *29*, 39–45.

Wilfling, F., Thiam, A.R., Olarte, M.-J., Wang, J., Beck, R., Gould, T.J., Allgeyer, E.S., Pincet, F., Bewersdorf, J., and Farese, R.V. (2014b). Arf1/COPI machinery acts directly on lipid droplets and enables their connection to the ER for protein targeting. Elife *3*, e01607.

Yang, H., Galea, A., Sytnyk, V., and Crossley, M. (2012). Controlling the size of lipid droplets: lipid and protein factors. Curr. Opin. Cell Biol. *24*, 509–516.

Zerial, M., and McBride, H. (2001). Rab proteins as membrane organizers. Nat. Rev. Mol. Cell Biol. *2*, 107–117.

STAR★METHODS

KEY RESOURCES TABLE

REAGENT or RESOURCE	SOURCE	IDENTIFIER
Chemicals, Peptides, and Recombinant Proteins		
Phospholipids	Avanti Polar Lipids	https://avantilipids.com/
Triolein	Sigma Aldrich	T7140
Cholesteryl oleate	Sigma Aldrich	C9253
Squalene	Sigma Aldrich	S3626
Triolein-pyrene	Markergene	M0258
Autotaxin inhibitor PF-8380	Sigma Aldrich	SML0715-5MG
Phospholipase A2 from bovine pancreas	Sigma Aldrich	P8913
Terbinafine hydrochloride	Sigma Aldrich	T8826-100MG
HiPerFect Transfection Reagent	Qiagen	301704
1-butanol	Sigma Aldrich	B7906
SCD1 Inhibitor	Caymanchemical company	CAY10566
DMEM 1X+GlutaMAX-1	ThermoFisher	319666-021
Mavalonic acid 5-phosphate trilithium	Alsachim	SVI-ALS-16-267
Farnesyl pyrophosphate	Sigma Aldrich	F6892-1VL
Triolein-pyrene 1,2-Dioleoyl-3-(pyren-1-yl)decanoyl-rac-Glycerol	Marker Gene (Technologies, Inc)	M0258
Oleic Acid	Sigma Aldrich	O1008
Methyl arachidonyl fluorophosphonate	Sigma Aldrich	SLBM8708V
Glyceryl trioctanoate	Sigma Aldrich	T 9126
Experimental Models: Cell Lines		
Human hepatocytes Huh7.5	Apath Missouri	APC 49
Hela Cells	Laboratoire de chimie de l'Ecole Normale Supérieure de Paris	N/A
Drosophila KC 167 cells	Dusseldorf University	N/A
Oligonucleotides		
LPCAT1 silencer Pre-designed siRNA sense GGCCAGUAAGUACGGGAAAtt anti-sense UUUCCCGUACUUACUGGCCtt	Ambion, ThermoFisher scientific	Cat#AM16708
Recombinant DNA		
ORF of PLA_2G4A	VIGENE Biosciences	Cat#CH809193
Software and Algorithms		
Matlab R2016a	Licence of the École Normale Supérieure	https://fr.mathworks.com
Fiji	Online	https://imagej.net/Fiji
Plot2	Online	http://apps.micw.org/apps/plot2/
Corse Grain IT	Online	https://github.com/CG-it
Adobe illustrator CS4	Licence of the École Normale Supérieure	
GraphPad Prism 7.0a	Licence of the École Normale Supérieure	https://graphpad.com/scientific-software/prism/

CONTACT FOR REAGENT AND RESOURCE SHARING

Further information and requests for reagents may be directed to, and will be fulfilled by, the Lead Contact, Abdou Rachid Thiam (thiam@lps.ens.fr).

METHOD DETAILS

Droplet Interface Bilayer Formation

Unless mentioned, in vitro experiments were performed in the following HKM buffer: 50 mM Hepes, 120 mM Kacetate, and 1 mM $MgCl_2$ (in Milli-Q water) at pH 7.4. For the preparation of the droplet interface bilayers, buffer-in-oil emulsion droplets were made using 10 μL HKM dispersed in 40 μL of the lipid oil phase (preparation of the oil phase is described below). The generated emulsion was placed on a glass coverslips coated with chlorotrimethylsilane to prevent the splashing of the aqueous droplets. For the determination of the triolein concentration in the droplet interface bilayer by fluorescence measurements, 5 % of triolein-pyrene was added to the triolein phase.

Preparation of the Oil Phase

Phospholipids used for droplet interface bilayers and artificial LDs formation were purchased from Avanti Polar Lipids, Inc. Chloroform which was dissolving the lipid was evaporated under a stream of argon; the dried lipids were subsequently re-solubilized to the desired concentration in the oil phase notably triolein (TO), trioctanoate, triolein-sterol ester (SE) mixture (TO-SE, 75/25, w/w), and squalene (SQ). Lipid concentrations ranging from 0.1 to 5% w/w were tested, all of which were above the critical concentration for forming stable droplet interface bilayers, i.e. no fusion between buffer droplets.

Droplet Interface Bilayer Angle and Bilayer Triolein Signal Determinations

The budding angle θ defined in Figure 2A is given by: $2\theta = \sin^{-1}(R_b/R_1) + \sin^{-1}(R_b/R_2)$, where R_b, R_1 and R_2 respectively denote for the radii of the bilayer and drops. The fluorescence intensity within the bilayer was measured as follows: $I = (L_1\text{-}L_2)/(L_3\text{-}L_2)$, where L_1 represents the fluorescence intensity of the bilayer, L_2 the background intensity which is the one of the drop, and L_3 is the reservoir signal of the surrounding triolein-pyrene phase.

Giant Unilamellar Vesicles and Artificial Lipid Droplets Formation

GUVs were prepared by electroformation. Phospholipids and mixtures thereof in chloroform at 0.5 μM was dried on an indium tin oxide (ITO)-coated glass plate. The lipid film was desiccated for 1 h. The chamber was sealed with another ITO- coated glass plate. The lipids were then rehydrated with a sucrose solution (275 mOsm). Electroformation is done using 100 Hz AC voltage at 1.0 to 1.4 Vpp and maintained for at least 1 h. This low voltage was used to avoid hydrolysis of water and dissolution of titanium ions glass plate. GUVs were either stored in the chamber at 4 °C overnight or directly collected with a Pasteur pipette.

To prepare the artificial lipid droplets artificial LDs 5 μL of the lipid oil solution was added to 45 μL of HKM buffer. The mixture was sonicated. The diameter of the resulting droplets is a few hundred nanometers. Guvs were then incubated with the artificial LDs for 5 min.

For LPC accumulation in GUVs mediated by phospholipase c-phospholipase A2, we first made GUVs containing 70/30 (mol/mol) PC/PA and incorporated artificial LDs. The presence of PA led to non-budded droplets. The GUVs - artificial LDs mixture was then placed on a glass coverslip pretreated with 3 % wt/v BSA and washed three times with buffer. Phospholipase A2 activity buffer (25 mM Hepes, 120 mM KCl, and 2 mM $MgCl_2$ in Milli-Q water at pH 8) was added to a final volume of 1 mL. Finally 50 μL of purified phospholipase A2 at 5 mg/mL followed by 150 μL of BSA 0,3 % wt/v was incorporated to the mixture, and observed during one hour at room temperature.

Measurement of the Interfacial Tension of the Interface of Artificial Droplets

Interfacial tension measurements were performed using a drop tensiometer device (Tracker, Teclis-IT Concept, France). The principle of the drop profile analysis is based on the determination of the shape of a liquid drop suspended in another liquid from a video image and its comparison with theoretical profiles calculated from the Gauss Laplace equation. In our case, the pendant drop is the neutral lipid phase, which contains the phospholipids, formed in the aqueous HKM buffer. Immediately, the tension decreases by the continuous absorption of phospholipids to the oil/water interface. Throughout the absorption kinetics, the drop area is maintained constant. Next, the drop is compressed by decreasing its volume (at a withdrawing speed of - 0,03 mm^3/s), until complete saturation of the interface is reached (marked by plateau of tension during compression). Each surface tension experiment was determined by this means and a minimum of 3 measurements was performed for each lipid condition studied.

Surface Tension Measurements by Microaspiration

The surface tensions of purified droplets and GUVs was measured using micromanipulation technique. The device was made up of a micromanipulator and a pipette holder (Narishige, Japan). Pipettes were incubated in a 5% bovine serum albumine (BSA) before use, in order to prevent droplet from adhering on the glass. As shown in Figure S1A, the micromanipulation of a single droplet (or GUV, Figure S4J) allows determining ST through the measurement of the pipette diameter, droplet diameter, and the minimal pressure at which the droplet formed a tongue length comparable to the pipette diameter (Thiam et al., 2013a):

$ST = P_{suc}/[2(1/R_p - 1/R_d)]$, with P_{suc}, R_p and R_g respectively being the suction pressure, the pipette radius and the droplet (GUV) radii. The different sizes were obtained by image analysis (ImageJ). The suction was carried out using a syringe. The resulting pressure was measured with a pressure transducer (DP103 provided by Validyne eng. corp, USA), the output voltage of which was monitored with a digital voltmeter. The pressure transducer (range 55 kPa) was calibrated prior to experiments.

Cellular Fractionation

Cells were harvested, washed with ice-cold PBS, re-suspended in 2 ml of PBS, sonicated (using a Soniprep 150, MSE, London, UK) for 3 cycles at 0°C and 50% cycle duty (0,5 s pulse rate) for 4 minutes. The lysate was sequentially centrifuged at 500 g for 5 minutes and 8 000 g for 15 minutes (at 4°C) to remove unbroken cells, nucleus and mitochondria. To purify LDs the 8 000 g supernatant was mixed with glycerol/HKM (70:30). The gradient was ultracentrifuged at 100 000 g for 1 h and the LDs were collected from the top fraction.

Lipid Extraction

Lipid extraction was performed as described by Folch. Under ventilated hood a pyrex tube containing 10 mL of methanol was heated in a water bath at 90°C. Then the supernatant was removed, the pellet was placed in the boiling methanol for 1-2 minutes then immediately immersed in an ice water bath. The mixture of extract and methanol was then transferred to a potter homogenizer containing 10 mL of chloroform (5 strokes) and left in the ice for 5 minutes. The mixture was introduced to the tube containing 6 ml of NaCl 9 g/L, vortexed several times and stored at 4°C overnight. The bottom layer (chloroform containing lipid extract) was collected with a Pasteur pipette in a pyrex tube. The extracts were concentrated using an evaporator under nitrogen and stored at −20 °C until required for analysis.

Thin Layer Chromatography and Lipid Detection

Lipids were extracted and separated on silica TLC plates (Merck) either in chloroform/methanol/acetone/acetic acid/water (100:20:40:20:10) for phospholipids or in petroleum ether/diethyl ether/acetic acid (90:10:1) for neutral lipids, and detected by iodine vapor staining. Bands were identified by comparison with standards.

Cellular Lipid Droplet Size Measurements

Cells were treated with a solution of 500 μM oleate complexed with BSA. Formed LDs were stained with BODIPY and subsequently imaged. The diameter of LDs was measured by using a customized ImageJ and Matlab hybrid program. A minimum of 25 cells was analyzed for each condition.

Cell Culture

Huh7 and Hela cells were maintained in Dulbecco's modified Eagle's medium (DMEM) supplemented with 10% heat inactivated fetal bovine serum (Life Tech- nologies), 4.5 gL^{-1} D-glucose, 0.1 gL^{-1} sodium pyruvate (Life Technologies) and 1% penicillin-streptomycin (Life Technologies). The cells were cultured at 37°C under a 5% CO2 atmosphere. Confluent monolayers of cells were re-suspended after trypsinization and plated into a 35 mm cell-culture Mattek dishes (with a glass coverslip at the bottom), (MatTek Corp. Ashland, MA).

Overexpression of Phospholipase A2

When indicated Hela cells (60-70% confluence) were transfected with 3 μg of plasmid/mL (PLA_2G4A) in pEnter, with C terminal Flag and His tag (VIGENE Biosciences) using Polyethylenimine HCl MAX (Polysciences, Inc) following the manufacturer's instructions. After 24 hrs transfection, cells were incubated with 500 μM oleic acid coupled to BSA to induce LD formation.

Enzymes Inhibitions

Inhibition of ATX/Lyso-PLD, by ATXi in LPCAT1_siRNA treated cells, was performed as following. siRNA transfection Silencer predesigned siRNAs directed against human LPCAT1 were used: sense GGCCAGUAAGUACGGGAAAtt and anti-sense UUUCCCGUA CUUACUGGCCtt (Ambion siRNA_LPCAT1, #127470, ThermoFisher scientific). Cells were transfected at 60-70% confluence by adding to each cell-culture Mattek disches 4μL of the stock siRNA solution (20 nM) and 3μL of HiPerFect Transfection Reagent (QIAGEN). After 24 hrs, ATXi that is the inhibitor of autotaxin, the enzyme that synthesizes Lyso-PA from Lyso-PC, was added to the culture medium 4 hrs. Next the cells were oleate loaded (500 μM) and analyzed 4 hrs later.

For phospholipase A2 and PLD double inhibition experiments, cells were pretreated with 15 μM of the c-phospholipase A2 inhibitor methyl arachidonyl fluorophosphonate (MAFP), and 0,5% v/v of the primary alcohol 1-butanol inhibitor of PLD for 30 min. Cells were next incubated with oleate for 8 hrs.

The pharmacological inhibition of SCD1 was achieved using SCD1 inhibitor ($SCD1_i$, #CAY10566). Huh7 cells were treated with 2.5 μM SCD_{1i} for 24 hours then oleate loaded for 24 hrs.

Induction of Squalene Accumulation

For squalene accumulation, terbinafine was used to inhibit the squalene epoxidase. Hela cells were treated with (a) 500 μM mevalonic acid and 20 μM farnesyl for 4 hrs (control), or with (b) 300 μM terbinafine for 1 hr prior to mevalonic acid and farnesyl treatment, or (c) treated with SCD_{1i} for 24 hrs, prior terbinafine treatment and mevalonic acid and farnesyl loading.

Relevance of Curvature for Lipid Droplet Budding (Related to Figures 1 and 2)

The deformation of a monolayer is mainly characterized by two parameters:

- The bending rigidity, which is the energy cost for bending the monolayer membrane. It is characterized by the bending rigidity κ, which works against curving the monolayer.
- The surface tension, γ, is the energy cost per generated area between two compartments; it works to decrease the total amount of surface between the compartments.

Budding is not immediately reached with the volume increase of a forming LD. A nascent lens is first reached as observed in cells (Choudhary et al., 2015).

The initial lens shape of a forming LD is owed in part to the bending rigidity of the monolayer, which tends to flatten the forming LD. This rigidity effect is indeed important at the beginning of LD formation because the nanometric scale of the LD induces important curvatures.

Under budding conditions, the monolayer surface tension has the opposite effect of minimizing the lens surface, to favor the formation of a spherical LD.

The monolayer bending rigidity and surface tension have thus antagonist contributions in the early steps of LD formation. There exist a characteristic length λ above which surface tension dominates (Thiam and Foret, 2016)

$$\lambda = \sqrt{\kappa/\gamma_c}$$

For a fluid phospholipid monolayer, κ is beneath $20k_BT$ (Kabalnov and Wennerström, 1996), and γ is $\sim 1 mN/m$, as for the purified cellular LDs (Figure 1A). Consequently:

$$\lambda \sim 10 - 20\, nm$$

Thus surface tensions dominate in budding when the droplet dimension is above 20 *nm*.

This result means that in the giant vesicles and artificial LD experiments (Figure 1), or in the droplet interface bilayer (DIB) (Figure 2), only surface tensions are into play. Curvature, which is inherent to the bending rigidity, is not relevant because the dimensions are well above 20 nm. The curvature of drops in the DIB system does not have effects on the budding angle, controlled by surface tensions.

Theoretical Modeling of the Shape of Lipid Droplet Budding (Related to Figure 5G)

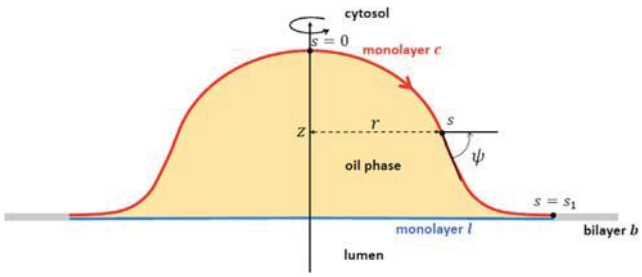

1. Model

A forming LD is considered as an oil phase embedded between two unzipped monolayers of a bilayer, see figure. In a continuous medium description, the monolayers and the bilayer are described as elastic fluid membranes, each characterized by its tension and bending rigidity.

In order to make our model as simple as possible and capture the main physical mechanism of LD budding, we assume that (*i*) the luminal LD monolayer *l* and the bilayer *b* are flat, (*ii*) the LD shape is symmetrical around the z-axis and, (*iii*) the spontaneous curvature of the monolayers is zero. Under these hypothesis, the shape of the LD is determined by the shape of the monolayer of the cytosol side *c* and is controlled by the following parameters: κ, the bending modulus of the monolayer *c*; γ_c, γ_l, and γ_b which are respectively the tensions of the monolayer *c*, the monolayer *l* and the bilayer *b*; the volume *V* of the oil droplet. The equilibrium shape corresponds to the minimum of the free energy:

$$F = \int \frac{\kappa}{2}(C_1 + C_2)^2 dA_c + \gamma_c A_c(\gamma_l - \gamma_b)A_l \qquad \text{(Equation 1)}$$

The first term is the bending elastic energy of the monolayer *l*, with *A* its area, and C_1 and C_2 its two principal curvatures. The next terms are the interfacial energies with A_c the area of the monolayer *c*.

2. Shape Equations

For axisymmetric membranes, the derivation of the equations governing the shape has been standardized; see for example (Foret, 2014; Julicher and Seifert, 1994; Seifert et al., 1991). Computing the shape reduces to compute the 1D contour at a given revolution angle. The position of a point on this contour is given by the arclength *s*. At the boundaries $s = 0$ (on the z-axis) and $s = s_1$ (where the two monolayers meet to form the bilayer). The shape of the contour can be fully characterized by $\psi(s)$, the angle between the tangent and radial vectors, see introductive figure. The functions $r(s)$ and $z(s)$ (see definition in the introductive figure) are then obtained by

integrating $r = \cos(\psi)$ and $z = -\sin(\psi)$, where the dots denote for the derivatives with respect to s. The two principal curvatures are $C_1 = \dot{\psi}$ and $C_2 = \sin(\psi)/r$; the surface element is $dA = 2\pi r ds$. The free energy then reads as follow:

$$F = 2\pi \int_0^{s_1} \left[(\kappa/2)\left(\dot{\psi} + \sin(\psi)/r\right)^2 + \gamma_c \right] r ds + (\gamma_l - \gamma_b)\pi r(s_1)^2 \qquad \text{(Equation 2)}$$

This energy is minimized with respect to $r(s)$ and $\psi(s)$ under the constraints that $\dot{r} = \cos(\psi)$ and,

$$V = \int_0^{s_1} \pi r^2 \sin(\psi) ds \qquad \text{(Equation 3)}$$

These constrains are accounted for by introducing the Lagrange multipliers $t(s)$ and p that is the droplet pressure. The functional to be minimized is then $S = F - pV + 2\pi \int_0^{s_1} t(s)(\dot{r} - \cos(\psi)) ds$, which can be written

$$S[r(s), \psi(s)] = 2\pi \int_0^{s_1} L\left(\psi, \psi, \dot{r}, r\right) ds + (\gamma_l - \gamma_b)\pi r(s_1)^2$$

$$\text{with} \quad L = (\kappa/2)\left(\dot{\psi} + \sin(\psi)/r\right)^2 r + \gamma_c r + (p/2) r^2 \sin(\psi) + t(\dot{r} - \cos(\psi)) \qquad \text{(Equation 4)}$$

The variation of S reads,

$$\frac{\delta S}{2\pi} = \int_0^{s_1} \left(\left(\frac{\partial L}{\partial \psi} - \frac{d}{ds}\frac{\partial L}{\partial \dot{\psi}} \right) \delta\psi + \left(\frac{\partial L}{\partial r} - \frac{d}{ds}\frac{\partial L}{\partial \dot{r}} \right) \delta r \right) ds - \left.\frac{\partial L}{\partial \dot{\psi}}\right|_0 \delta\psi(0) + \left.\frac{\partial L}{\partial \dot{\psi}}\right|_{s_1} \delta\psi(s_1) - \left.\frac{\partial L}{\partial \dot{r}}\right|_0 \delta r(0) + \left(\left.\frac{\partial L}{\partial \dot{\psi}}\right|_{s_1} + (\gamma_l - \gamma_b) r(s_1) \right) \delta r(s_1) - H \delta s_1$$

(Equation 5)

with

$$H = \frac{\partial L}{\partial \dot{\psi}} \dot{\psi} + \frac{\partial L}{\partial \dot{r}} \dot{r} - L = constant$$

At equilibrium, $\delta S = 0$, each term must vanish, which leads to

$$\frac{\partial L}{\partial \psi} - \frac{d}{ds}\frac{\partial L}{\partial \dot{\psi}} = 0 \; and \; \frac{\partial L}{\partial r} - \frac{d}{ds}\frac{\partial L}{\partial \dot{r}} = 0$$

which gives the equations governing the shape,

$$\begin{aligned} \dot{r} &= \cos(\psi) \quad \dot{\psi} = u \quad \dot{t} = \frac{\kappa}{2}u^2 - \frac{\kappa}{2}\frac{\sin^2(\psi)}{r^2} + \gamma_c - pr\sin(\psi) \\ \dot{u} &= -\frac{u\cos(\psi)}{r} + \frac{\cos(\psi)\sin(\psi)}{r^2} + \frac{p}{2\kappa} r\cos(\psi) + \frac{t\sin(\psi)}{\kappa r} \end{aligned} \qquad \text{(Equation 6)}$$

At the boundaries, $\psi(0) = \psi(s_1) = r(0) = 0$ so that $\delta\psi(0) = \delta\psi(s_1) = \delta r(0) = 0$ in (5). The radius of the droplet basis $r(s_1)$ is not fixed a priori but adjusts itself to minimize the energy. According to (5), $r(s_1)$ is such that

$$\left.\frac{\partial L}{\partial \dot{\psi}}\right|_{s_1} + (\gamma_l - \gamma_b) r(s_1) = 0$$

Finally, the length of the contour s_1 is not fixed and thus, according to (5), $H = 0$, which implies $t(0) = 0$. In summary, the boundary conditions are,

$$\psi(0) = 0\,, \quad r(0) = 0\,, \quad t(0) = 0, \quad \psi(s_1) = 0\,, \quad t(s_1) = (\gamma_b - \gamma_l) r(s_1) \qquad \text{(Equation 7)}$$

Solving the shape equations with the boundary conditions gives the equilibrium shape for a given pressure p. This pressure has to be adjusted to obtain the shape with the prescribed volume V.

3. Dimensionless Equations and Numerical Implementation

The natural length scale of this system is

$$\lambda = \sqrt{\frac{\kappa}{\gamma_c}} \qquad \text{(Equation 8)}$$

For droplet with $V \gg \lambda^3$, the bending rigidity of the monolayer should have a negligible effect on the droplet shape, which should be mainly determined by the competition of the surface tensions.

By using λ as the length unit and κ as the energy unit, and doing the variable changes,

$$\frac{s}{\lambda}\rightarrow s\ ,\quad \frac{r}{\lambda}\rightarrow r\ ,\quad \frac{z}{\lambda}\rightarrow z\ ,\quad \frac{t\lambda}{\kappa}\rightarrow t\ ,\qquad \frac{F}{\kappa}\rightarrow F\ ,\qquad \frac{p\lambda^3}{\kappa}\rightarrow p \tag{Equation 9}$$

one obtains the dimensionless shape equations,

$$\dot{r}=\cos(\psi);\ \dot{\psi}=u;\ \dot{t}=\frac{1}{2}u^2-\frac{1}{2}\frac{\sin^2(\psi)}{r^2}+1-pr\sin(\psi);\ \dot{u}=-\frac{u\cos(\psi)}{r}+\frac{\cos(\psi)\sin(\psi)}{r^2}+\frac{p}{2}r\cos(\psi)+\frac{t\sin(\psi)}{r} \tag{Equation 10}$$

and the boundary conditions,

$$\psi(0)=0\ ,\quad r(0)=0\ ,\quad t(0)=0,\quad \psi(s_1)=0\ ,\quad \frac{t(s_1)}{r(s_1)}=\frac{\gamma_b-\gamma_l}{\gamma_c} \tag{Equation 11}$$

The shape is thus controlled by only two dimensionless parameters: p, which is adjusted to have the correct volume, and $(\gamma_b-\gamma_l)/\gamma_c$, which is nothing but the cosine of the contact angle (the angle that would form the droplet at the monolayer junction in the absence of bending rigidity).

Numerically, the four first order differential equations are integrated with an adaptive step Runge-Kutta algorithm, from the point $s = 0$ until the point s_1 such that $\psi(s_1) = 0$.

The initial condition $u(0)$ is not known and is tuned until the shape is such that the last boundary condition $t(s_1)/r(s_1) = (\gamma_b - \gamma_l)/\gamma_c$ is satisfied (this is a so-called ''shooting'' method). The pressure p is then tuned to obtain the chosen volume.

For a range of the control parameters V and $(\gamma_b - \gamma_l)/\gamma_c$, several solutions of the shape equations are found, *i.e.* the boundary condition for $t(s_1)/r(s_1)$ is satisfied for different values of $u(0)$ leading to different possible shapes. The correct shape is selected as the one that has the lowest free energy.

For other ranges of the control parameters, no solutions are found. Yet, the spherical shape with an infinitely narrow neck connecting the membrane is still a possible solution (not accessible numerically) and is the only possible shape in this case. This corresponds to the ''budding'' region of the phase diagram.

In the ''wetting'' region of the phase diagram, the shapes are ''spread'' in the sense that they have $\psi < \pi/2$ everywhere. In the yellow region, the shapes correspond to a partially budded droplet with a neck region ($\psi > \pi/2$ for some s).

Molecular Dynamics (MD) Simulations (Related to Figures 4C–4E)

MD simulations were performed using the coarse-grain (CG) lipid model by Klein and coworkers (Shinoda et al., 2007; Bacle et al., 2017). The simulations were performed with the software LAMMPS, and all molecular graphics were generated with visual molecular dynamics (Humphrey et al., 1996). Configurations for the various CG systems were generated by converting atomistic snapshots using the CG-it software (https://github.com/CG-it).

In LAMMPS, pressure and temperature were controlled using a Nosé-Hoover thermostat and barostat, with target temperature and pressure of 300 K and 1 atm, respectively. The lateral *xy* dimensions of the systems were constrained to be equal, while the orthogonal dimension *z* was allowed to fluctuate independently. For simulations at non-zero surface tension, the *xy* lateral dimensions were kept fixed. Van der Waals and electrostatics were truncated at 1.5 nm, with long-range electrostatics beyond this cutoff computed using the particle-particle-particle-mesh (PPPM) solver with an RMS force error of 10^{-5} kcal mol^{-1} Å^{-1} and order 3. In all simulations, a time step of 20 fs was used.

For the ''blister formation'' simulations, a box consisting of 50 PC molecules and a variable number of TO molecules corresponding to the different TO concentrations was initially prepared. The two PC monolayers were displaced along the *z*-axis in order to allow the insertion of the TO molecules without any steric contact between the molecules. The TO molecules were subsequently randomly placed between the two monolayers. The box was then replicated 8 times along the *x* and *y* axis for a total of 3200 PC molecules in each system. For each concentration 3 independent simulations were performed. The simulations were stopped when blister formation was observed. When no blister formation was observed, the simulations were stopped after 1.5 μs. Error bars are given as standard deviations over the three independent simulations.

For the ''triglyceride diffusion'' simulations, a system composed of 204 TO molecules in the liquid state was placed between two monolayers of 625 PC molecules each, for a total of 1250 PC molecules. After 1 ns of equilibration to let the two monolayers spontaneously form a bilayer without any leakage of TO molecules from the blister, MD simulations of 1.5 μs were performed at different fixed values for the (x,y) coordinates, resulting in different surface tensions. Analyses were performed on the last 1 μs of the MD run. Error bar are given as standard deviation over the last 1 μs.

In all cases, a TO blister was defined as all TO molecules that are within 2.5 nm of distance of the ''core'' TO molecules, i.e. those that are not within 2.5 nm of any PC phosphate group. The ''free bilayer'' for the analysis of the triglyceride diffusion was defined as the bilayer that was not outside the computed initial area of the TO blister after equilibration (the blister radius was determined to be 7 nm).

Lateral pressure and density profiles were computed for a system composed of 3200 PC molecules, with or without 4% TO molecules. The simulations were run for 800 ns and analyses were performed on the last 300 ns.

Lateral pressure profiles (LPPs) $p(z)$ were computed by evaluating, following the protocol described in (Ding et al., 2015):

$$p(z) = P_L(z) - P_N$$

where $P_L(z)$ is the lateral component of the pressure tensor $P_L(z) = \frac{1}{2}(P_{xx}(z) + P_{yy}(z))$ and P_N the normal component ($P_N = P_{zz}$).

A negative $p(z)$ means the system wants to shrink the lateral dimension, a positive $p(z)$ means the system wants to expand the lateral dimension.

Density profiles were computed by averaging the mass density of the various molecules along the z-axis using a grid of 0.1 nm resolution.

For all simulations, surface tension was computed from the diagonal values of the pressure tensor (P_{xx}, P_{yy}, and P_{zz}) using the Kirkwood-Irving method:

$$g = \frac{L}{2}\left\langle P_{zz} - \frac{1}{2}(P_{xx} + P_{yy})\right\rangle$$

where L is the box length in the z dimension and <> means an ensemble average.

QUANTIFICATION AND STATISTICAL ANALYSIS

For statistical evaluation of LD size variation due to the modulation of enzymes vs. control (in Figures 6E, 6H, 6K, 6O, S6H, and S6L), the data was assessed by d'Agostino & Pearson omnibus normality test. All data followed a non Gaussian distribution. Statistical significance was evaluated by Kolmogorov-Smirnov test using Prism software. Data are presented with the 10-90% box-and-whisker plot, where the central box represents the interquartile ranges (25th to 75th percentiles), the middle line represents the median sample value, and the horizontal lines represent the minimum and the maximum value of observation range.

The statistical comparisons of the contact angles for the lipid surfactants were done by Mann–Whitney non-parametric test (in Figure 2E). All values shown in the text and figures are mean ± S.D., where N=10. Values are from at least 3 independent experiments.

(*** indicates $p < 0.0001$ ** indicates $p < 0{,}001$ * indicates $p < 0.01$).

DATA AND SOFTWARE AVAILABILITY

Computation of the model was done using C++. Simulation was carried on by using the CG-it software (https://github.com/CG-it).